Electronic sensor and actuator webs for large-area complex geometry cardiac mapping and therapy

Dae-Hyeong Kim[a,1], Roozbeh Ghaffari[b,1], Nanshu Lu[c,1], Shuodao Wang[d,1], Stephen P. Lee[b], Hohyun Keum[e], Robert D'Angelo[b], Lauren Klinker[b], Yewang Su[d,f], Chaofeng Lu[d,g], Yun-Soung Kim[e], Abid Ameen[e], Yuhang Li[d,h], Yihui Zhang[d,f], Bassel de Graff[b], Yung-Yu Hsu[b], ZhuangJian Liu[i], Jeremy Ruskin[j], Lizhi Xu[e], Chi Lu[e], Fiorenzo G. Omenetto[k], Yonggang Huang[d], Moussa Mansour[j], Marvin J. Slepian[l], and John A. Rogers[e,2]

[a]Center for Nanoparticle Research of Institute for Basic Science, World Class University Program of Chemical Convergence for Energy and Environment, School of Chemical and Biological Engineering, Seoul National University, Seoul 151-742, Korea; [b]MC10 Inc., Cambridge, MA 02140; [c]Department of Aerospace Engineering and Engineering Mechanics, University of Texas at Austin, Austin, TX 78712; [d]Departments of Mechanical Engineering and Civil and Environmental Engineering, Northwestern University, Evanston, IL 60208; [e]Department of Materials Science and Engineering, University of Illinois at Urbana–Champaign, Urbana, IL 61801; [f]Center for Mechanics and Materials, Tsinghua University, Beijing 100084, China; [g]Soft Matter Research Center and Department of Civil Engineering, Zhejiang University, Hangzhou 310058, China; [h]School of Astronautics, Harbin Institute of Technology, Harbin 150001, China; [i]Institute of High Performance Computing, A*Star, Singapore 138632; [j]Cardiac Arrhythmia Unit, Massachusetts General Hospital, Boston, MA 02140; [k]Department of Biomedical Engineering, Tufts University, Medford, MA 02155; and [l]Departments of Medicine and Biomedical Engineering, Sarver Heart Center, University of Arizona, Tucson, AZ 85724

Edited by Kevin Kit Parker, Harvard University, Cambridge, MA, and accepted by the Editorial Board October 17, 2012 (received for review April 7, 2012)

Curved surfaces, complex geometries, and time-dynamic deformations of the heart create challenges in establishing intimate, nonconstraining interfaces between cardiac structures and medical devices or surgical tools, particularly over large areas. We constructed large area designs for diagnostic and therapeutic stretchable sensor and actuator webs that conformally wrap the epicardium, establishing robust contact without sutures, mechanical fixtures, tapes, or surgical adhesives. These multifunctional web devices exploit open, mesh layouts and mount on thin, bio-resorbable sheets of silk to facilitate handling in a way that yields, after dissolution, exceptionally low mechanical moduli and thicknesses. In vivo studies in rabbit and pig animal models demonstrate the effectiveness of these device webs for measuring and spatially mapping temperature, electrophysiological signals, strain, and physical contact in sheet and balloon-based systems that also have the potential to deliver energy to perform localized tissue ablation.

flexible electronics | semiconductor nanomaterials | stretchable electronics | implantable biomedical devices | cardiac electrophysiology

Cardiac arrhythmias occur in all component structures and 3D regions of the heart, resulting in significant challenges in diagnosis and treatment of precise anatomic targets (1). Many common arrhythmias, including atrial fibrillation and ventricular tachycardia, originate in endocardial substrates and then propagate in the transverse direction to affect epicardial regions (1, 2). Characterizing arrhythmogenic activity at specific regions of the heart is thus critical for establishing the basis for definitive therapies such as cardiac ablation (3). Advanced tools that offer sufficient spatial resolution (<1 mm) and intimate mechanical coupling with myocardial tissue, but without undue constraints on natural motions, would therefore be of great clinical importance (4–6). To date, cardiac ablation procedures have largely relied on point ablation catheters deployed in the endocardial space (1, 5, 7–9). Although successful in the treatment of simple arrhythmias originating in and around the pulmonary veins, these devices are poorly suited for treating complex arrhythmias, such as persistent atrial fibrillation (10–13), that arise from various sites inside the left atrium. Other classes of devices have demonstrated the utility of spatiotemporal voltage mapping using various modes of operation, including noninvasive surface mapping designs (14, 15), epicardial voltage-mapping "socks" (16–20), and endocardial contact and noncontact catheters, with densities approaching 64 electrodes (21–31). These solutions all exploit arrays of passive metal wire-based electrodes integrated on wearable vests and socks (14–20) or catheter systems (21–26) for mapping of complex arrhythmias. Building such mesh structures requires manual assembly and is only possible because the individual wires are millimeter scale in diameter and thus sufficiently large to be threaded to form a mesh. For catheter systems, the large size of individual electrodes gives rise to scalability challenges and interfacial mismatches between the mechanical properties and density of conventional passive electrode formats and that of soft, deformable cardiac tissue. Moreover, passive wire electrodes are largely limited to electrical sensing, without providing simultaneous feedback about mechanical and thermal properties; they are also incapable of providing more advanced forms of functionality that demand semiconductor devices as sensors or processing elements.

A much more powerful approach would exploit full, integrated circuits in intimate contact with the affected regions for evaluation in a parallel mode, at high sampling rates and high resolution, providing direct insight into the complex electrical, mechanical, and thermal properties of cardiac structures at the cellular level. The practical challenge is in interfacing the hard, planar forms of electronics that exist today with the soft, curvilinear, and time-dynamic surfaces of the heart, in a way that provides intimate, nondestructive contact, without slippage at the biotic/abiotic interface. Recent advances in nanomaterials research have established versatile strategies in mechanics designs and manufacturing techniques for high-quality electronics that can flex, twist, and stretch in ways that facilitate integration with biology (32). The most basic of these technologies (6, 33) was recently demonstrated in thin, flexible sheets of electronics that laminate on certain areas of the heart to provide unmatched capabilities in electrophysiological mapping. Although this format is effective for measuring small regions or those with modest curvature, it is incapable of large-scale evaluation or integration with epicardial areas around the apex or in structured regions across the atrioventricular groove between the ventricles, owing to the inability of flexible sheets to wrap and conform to the complex topographies of the heart. Complex endocardial surfaces within the atria and ventricles pose even greater challenges for intimate soft contact.

Ultra-low modulus, stretchable sensor and actuator webs overcome the limitations of previously described cardiac and

---

Author contributions: D.-H.K., R.G., N.L., S.W., S.P.L., H.K., F.G.O., M.J.S., and J.A.R. designed research; D.-H.K., R.G., N.L., S.W., H.K., R.D., L.K., Y.-S.K., A.A., B.d.G., Y.-Y.H., L.X., Chi Lu, M.J.S., and J.A.R. performed research; D.-H.K., R.G., N.L., S.W., S.P.L., R.D., L.K., Y.S., Chaofeng Lu, and J.A.R. contributed new reagents/analytic tools; D.-H.K., R.G., N.L., S.W., R.D., L.K., Y.S., Chaofeng Lu, Y.L., Y.Z., Z.L., J.R., Y.H., M.M., M.J.S., and J.A.R. analyzed data; and D.-H.K., R.G., N.L., S.W., and J.A.R. wrote the paper.

Conflict of interest statement: R.G., M.J.S., and J.A.R. are co-founders of MC10 Inc.

This article is a PNAS Direct Submission. K.K.P. is a guest editor invited by the Editorial Board.

[1] D.-H.K., R.G., N.L., and S.W. contributed equally to this work.

[2] To whom correspondence should be addressed. E-mail: jrogers@illinois.edu.

This article contains supporting information online at www.pnas.org/lookup/suppl/doi:10.1073/pnas.1205923109/-/DCSupplemental.

brain mapping sheets to allow intimate integration with the skin, even on highly irregular, wrinkled regions (34). In this case, a soft elastomeric film provides a supporting substrate in an overall design that offers equivalent mechanical properties that are matched to epidermis. The ability to conform to a dynamically deforming substrate like the heart poses significant new challenges compared with the brain and skin, which undergo significantly smaller levels of continuous deformations than the heart. Straightforward use of this technology for cardiac applications is thus frustrated, both by the highly time-dynamic motions associated with beating of the heart and by the need to wrap substantial regions of its surface. The biology itself (i.e., the heart) might, however, have the capacity to serve as the stretchable substrate in a manner similar to the static surface of the brain (35).

In this article we report a class of electronics that adopts this design in the form of epicardial webs, to provide (*i*) exceptionally low effective stiffness and high degrees of deformability, to yield negligible mechanical constraints on the natural motions of the heart and an ability to wrap large areas and complex contours, (*ii*) robust adhesion of sensor and actuator devices (located at the nodes of the mesh) to the epicardial surface simply by capillary interactions associated with the moist surface of the tissue, even under full dynamic motion associated with beating, (*iii*) open access of the vast majority of the tissue for introduction of bio-fluids, drugs, or other device probes, and (*iv*) direct visual and optical interrogation, for spectroscopic and/or microscopic measurement. The following results demonstrate this technology in a collection of sensor arrays that can measure electrical activity, temperature, mechanical strain, pressure, and physical contact on sheet and balloon-based platforms. Detailed modeling of the mechanics and in vitro and in vivo evaluations on animal models illustrate the underlying physics and potential clinical utility.

Results and Discussion

The web incorporates interconnects with filamentary serpentine shapes that join small sensor or actuator pads, all with ultrathin construction (<5 μm) and neutral mechanical plane configuration. Fig. 1 *A–C* shows designs and pictures of a representative epicardial web for electrophysiological mapping. The fabrication involves microelectronic processing techniques to create patterns of sensors and actuators that are lifted onto a sacrificial silk film and mounted onto the surface of the heart (Fig. 1 *D–F*). The silk film dissolves within minutes after exposure to moisture, leaving the web as a conformal, functional laminate on the heart. The systems stretch to ∼20% or more with minimum mechanical resistance (Fig. 1*C*).

Measurement of differential bipolar potentials during movements of the heart demonstrates essential functions in locating arrhythmogenic activity (Fig. 1 *G* and *H*). Rapid motions associated with cardiac contraction exert lateral forces on the web but cause little change in electrical performance because of the ability of the structures to naturally couple with the underlying cardiac tissue (Fig. 1 *E* and *F*). Surface tension due to tissue hydration provides further mechanical stability to ensure that the measuring sensors maintain contact at fixed positions. In vitro stretching experiments on centimeter-scale segments of muscle tissue excised

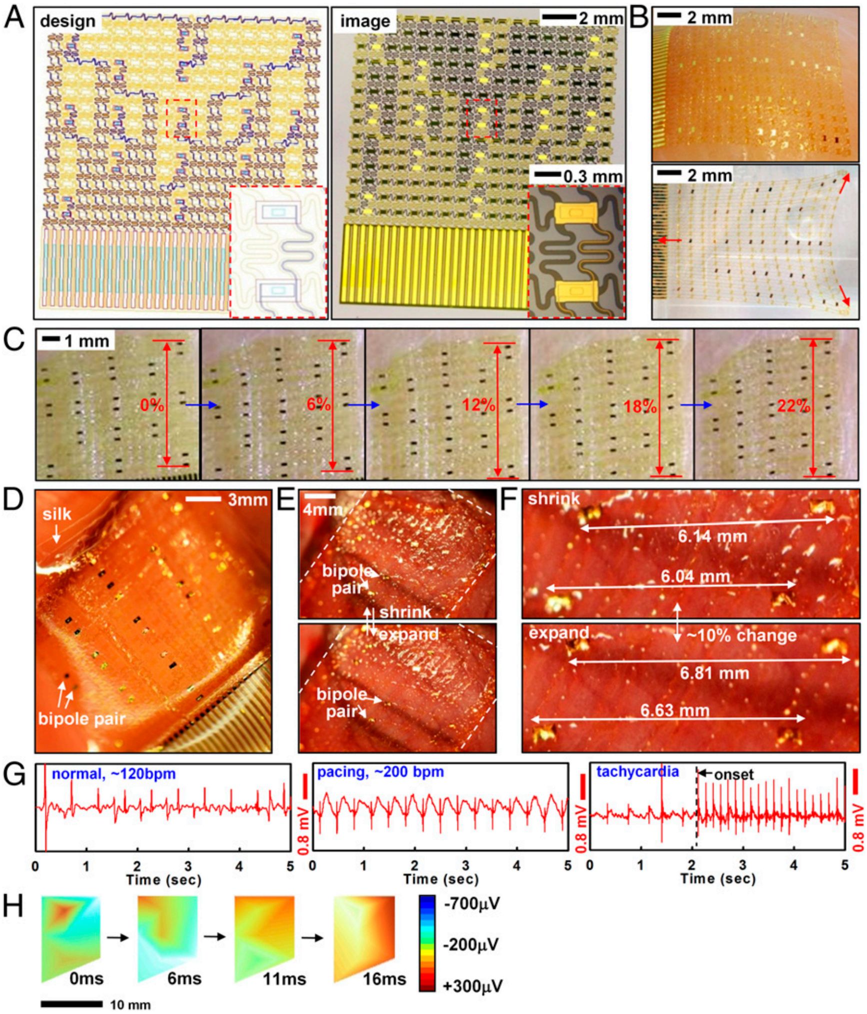

Fig. 1. Sensor web designed for epicardial EGM mapping. (*A*) Layout (*Left*) and corresponding picture (*Right*) of a web. (*Insets*) Magnified views of a pair of electrodes. (*B*) Optical image of a web after lamination onto tissue followed by dissolution of the silk substrate (*Upper*) and in free-standing form in a stretched configuration (*Lower*). (*C*) In vitro stretching experiment of a web on chicken meat with no slippage up to ∼22% strain. (*D*) Web on a silk substrate and after mounting on the epicardial surface (*E*). (*F*) Magnified image of interconnected electrodes moving synchronously with the underlying tissue. (*G*) Recorded EGM from electrodes during normal rhythm (*Left*), rapid pacing at ∼200 bpm (*Center*), and during tachycardia (*Right*). (*H*) EGM activation mapping at several time intervals, showing a depolarization wave front. The right frame provides color scales for potentials.

from chicken (*Gallus gallus domesticus*) torso show minimal slipping of devices relative to the tissue, in response to ~22% applied strains (Fig. 1*C*). Detailed layouts, cross-sectional designs, and fabrication strategies are provided in *SI Appendix* and Fig. S1. The same basic concepts and procedures may be used for diverse classes of sensors, as described in the next section.

Quantitative mechanics models (*SI Appendix*, Fig. S2) guide choices of web layout according to the elastic properties of the soft tissue and the nature of the interfacial contact. Three issues are of primary importance: (*i*) the effective stiffness of the web, (*ii*) the static adhesion forces that drive its conformal contact with the tissue, and (*iii*) interfacial friction forces that limit slippage of the nodes across the epicardial surfaces during motion. First, the tensile ($\overline{EA}_{\mathrm{mesh}}$) and bending stiffness ($\overline{EI}_{\mathrm{mesh}}$) can be obtained analytically in terms of the island and interconnect material properties and geometric configuration (*SI Appendix*, Fig. S1*C*). In particular, for the devices of Fig. 1, analysis yields $\overline{EA}_{\mathrm{mesh}} = 16$ N/m and $\overline{EI}_{\mathrm{mesh}} = 0.33$ nN-m, in good agreement with finite element analysis (FEA). Furthermore, $\overline{EA}_{\mathrm{mesh}}$ is reduced even further to values as low as 0.01 N/m, upon noncoplanar buckling of interconnects, as in *SI Appendix*. These values are exceptionally small compared with cardiac tissue, which has $\overline{EA}_{\mathrm{cardiac}} = 76$ N/m and $\overline{EI}_{\mathrm{cardiac}} = 23$ μN-m for 1.9-mm-thick ventricular walls (36) and an elastic modulus of $E_{\mathrm{heart}} = 40$ kPa (37). By comparison with previously reported active cardiac and neural mapping sheets [bending stiffness 31 N-m (6)], the web devices presented in this study are 5 orders of magnitude softer and comparable to passive devices used on the brain (34).The most favorable epidermal electronics had values of $\overline{EA} = 4.2$ N/m and $\overline{EI} = 0.3$ nN-m (35). The peak strains in webs during motion are also exceptionally small. For a full cycle of contraction to expansion during normal beating of the heart (~10% strain in both directions; *SI Appendix*, Fig. S2*C*), FEA gives maximum strains of 0.12% and 0.0091% in the polyimide and gold layers of electrodes and interconnects (*SI Appendix*, Fig. S2 *D* and *E*), with no slippage of the web on the heart.

The second mechanics issue relates to intimate coupling between electrodes (widths of $L \times L$) and the heart, approximated as a sphere with radius R_{heart}. For stable wrapping, the adhesion energy must overcome the increase in elastic energy due to global deformation of the web. This criterion can be described by the following analytical form (*SI Appendix*, Eq. **S1**):

$$\frac{L^2\overline{EI}_{\mathrm{mesh}}}{\gamma A R_{\mathrm{heart}}^2} + \frac{\pi \overline{EA}_{\mathrm{mesh}}}{\gamma A}\int_0^{L/\sqrt{\pi}}\left(1-\frac{R_{\mathrm{heart}}}{r}\sin\frac{r}{R_{\mathrm{heart}}}\right) r\,dr < 1, \qquad [1]$$

where γ and A are the work of adhesion and contact area between arrays and the moist surface of the heart, respectively. For experimental data of $L = 20$ mm, $R_{\mathrm{heart}} \sim 25$ mm, $\gamma \sim 0.1$ N/m (38–40), $A = 125$ mm^2 and the calculated $\overline{EA}_{\mathrm{mesh}}$ (~16 N/m) and $\overline{EI}_{\mathrm{mesh}}$ above, the left-hand side of Eq. **1** (~0.01) is 2 orders of magnitude smaller than 1. Consequently, the web should maintain good conformal contact with the heart during expansion and contraction (~10% change in R_{heart}).

Locally, electrode islands are in a periodic arrangement (Fig. 1 *A* and *B*). The energy release rate G for interfacial bonding between islands and a deforming substrate is given by (41) (*SI Appendix*):

$$G = \frac{E_{\mathrm{heart}}\varepsilon^2 w_y}{8}\tan\frac{\pi w_x}{2L_{\mathrm{unit}}}, \qquad [2]$$

where $\varepsilon \sim \pm 10\%$ is the approximate maximum expansion/contraction of the heart, E_{heart} is the Young's modulus of the heart, L_{unit} is the length of a representative unit cell of the electrode array (*SI Appendix*, Fig. S2*C*), and w_x and w_y are sizes of the island (*SI Appendix*, Fig. S2*C*). Electrode islands will remain intact with the heart during beating, provided that $G < \gamma$, where $\gamma \sim 0.1$ N/m (38–40) is the interfacial work of adhesion between the electrode and the heart. For experimental data of $w_x = 560$ μm, $w_y = 290$ μm, $L_{\mathrm{unit}} = 1.0$ mm, Eq. **2** gives $G = 0.022$ N/m, which is smaller than γ, and therefore, locally, there is no delamination between islands and the heart surface. For a larger stretch of $\varepsilon \sim 20\%$ as in Fig. 1*C*, $G = 0.088$ N/m given by Eq. **2** is still smaller than the interfacial adhesion, consistent with experiments (no interfacial delamination).

The third aspect relates to dynamic frictional forces at the interface, and their critical role in preventing relative slip of sensor/actuator nodes on the heart during beating. Webs expand/contract during heart motion, depending on the ability of interconnects to stretch and compress. The resulting maximum force acting on each island is obtained as $F_{\mathrm{pull}} = \overline{EA}_{\mathrm{mesh}}\varepsilon L_{\mathrm{unit}} g_1\left(\frac{\overline{EA}_{\mathrm{mesh}}}{E_{\mathrm{heart}}w_x}, \frac{w_y}{w_x}, \frac{w_x}{L_{\mathrm{unit}}}, \nu\right)$ by considering equilibrium between the island, interconnect, and the heart, where the function g_1 is given analytically in *SI Appendix*, ν is the Poisson's ratio of the heart. Because the web mounts on the epicardial surface without adhesives, the cumulative interface frictional force can be considered as the sum of such forces at each electrode, $f = \mu \cdot p_{\mathrm{air}} \cdot w_x \cdot w_y$, where μ is the coefficient of friction and p_{air} is the atmospheric pressure. To avoid slipping, $F_{\mathrm{pull}} < f$, in other words,

$$\frac{\overline{EA}_{\mathrm{mesh}}\varepsilon L_{\mathrm{unit}}}{\mu p_{\mathrm{air}} w_x w_y} g_1\left(\frac{\overline{EA}_{\mathrm{mesh}}}{E_{\mathrm{heart}}w_x}, \frac{w_y}{w_x}, \frac{w_x}{L_{\mathrm{unit}}}, \nu\right) < 1. \qquad [3]$$

The experimental parameters are $p_{\mathrm{air}} = 1.0$ atm, $w_x \times w_y = 560 \times 290$ μm^2, $L_{\mathrm{unit}} = 1.0$ mm, and $\nu = 0.45$ (37). Literature reports suggest that $\mu \sim 1.6$ with certain values that are an order of magnitude smaller (42). Eq. **3** holds over this range such that the electrode array does not slide because buckling of interconnects exerts much smaller pulling force on islands. With these values and $\overline{EA}_{\mathrm{mesh}} = 16$ N/m (before the interconnects buckle), the left-hand side of Eq. **3** (~0.05) is roughly 20 times lower than 1, indicating that slip effects are marginal during the beating cycle of the heart. This prediction is consistent with experimental findings (Fig. 1*C*) with no slippage up to ~22% strains, limited only by damage in tissues at higher strains.

Electrogram (EGM) recordings from the anterior ventricular surfaces validate the favorable mechanics and interface properties of the web design. Images collected during cardiac contractions (Fig. 1 *E* and *F*) show ~10% strains, without any noticeable slippages. Fig. 1*G* shows EGMs recorded from bipolar electrodes during normal rhythm [~120 beats per minute (bpm), *Left*], external pacing (~200 bpm, *Center*), and during abnormal rhythms (tachycardia, *Right*). The differential potentials measured across multiple electrodes can be converted into voltage color maps to reveal activation patterns using the onset and timing of activation across multiple sensors spaced across ~2 cm^2 surface (Fig. 1*H*). Although it is difficult to assess directionality of wave fronts as in optical mapping in vitro studies, webs containing 17 electrodes over the anterior surface of the heart were sufficient for isopotential voltage maps in vivo. We applied Delaunay triangulation to fit a surface to the electrode potentials measured across the array. The surface passed through the midpoint of each bipolar electrode and was linearly interpolated between individual nodes. Alternatively, single-ended voltage recordings and their differentials could provide further insight into activation patterns and directionality of wave fronts (43). These cardiac webs can be fabricated with dimensions suitable to characterize electrical activity of significantly larger human hearts by using similar procedures, but implemented with modern silicon (Si) foundries (12 in Si wafer technology) or flat panel display (glass substrate) manufacturing strategies. The number of wires for addressing the sensors may also be minimized via multiplexing schemes that exploit Si nanomembrane (NM) transistors as switching elements (6, 33).

In addition to electrical mapping, temperature sensors with similar designs can be used to map thermal activity during radiofrequency (RF) and cryo-ablation. Thermal and electrical activity monitoring during the delivery of pacing and ablation energy are powerful capability sets, that when offered in a single platform could enhance the safety and efficacy of cardiac ablation. Local EGM mapping reveals the electrical activity at a specific anatomical target and mapping of temperature distribution during energy delivery, then ensures adequate lesion characterization laterally and in the transverse directions. This form of thermography in epicardial web formats provides useful functionality to assess lesion formation. The same design strategies that apply to EGM electrodes are relevant to microfabricated thermistor arrays consisting of Ti/Pt (5/50 nm) thermal detectors (Fig. 2 *A* and *B* and *SI Appendix*, Fig. S3). Minimal leakage current in saline solution validates the reliability of encapsulation schemes (*SI Appendix*, Fig. S4). A ~40-mm^2 cylindrical section (radius ~3.5 mm) of dry ice placed on the center of the array and then removed after ~2.4 min simulates a cryoablation event, as illustrated by the dotted circle in Fig. 2*B*. RF energy delivered by a point electrode located near the array of temperature sensors demonstrates functionality in this context. Images of resulting lesions for each process appear in Fig. 2*C*. Calibration results of temperature sensors appear in Fig. 2*D* (normalized R, i.e., R/R$_0$) and Fig. 2*D*, *Inset* (raw R, i.e., R), respectively. Fig. 2*E* shows the changes in temperature measured at individual sensor nodes during cryoablation. Sensors located close to the source register temperatures as low as −48 °C (Fig. 2*E*); those at millimeter distances show higher temperatures. More details for thermal sensing capability are in *SI Appendix*.

Models of heat conduction can determine expected temperature distributions (*SI Appendix*, Fig. S5*A*). The ventricular wall of the rabbit heart has a nominal thickness h = 1.9 mm, thermal conductivity $k = 0.512$ W/m/K (44), and a thermal diffusivity $\alpha = 0.131$ mm^2/s (45). Computed variations in surface temperature are consistent with experimental findings over the entire time range (~3 min) without parameter fitting (*SI Appendix*, Fig. S5*B*). At t = 2.4 min, the temperature exceeds that for successful lesion (~−50 °C) over a region with diameter ~8.2 mm and depth ~1.9 mm around the dry ice (Fig. 2*F*). The same device can also monitor elevated temperatures in RF ablation (*SI Appendix*, Fig. S6*A*). The model predicts temperature distributions that are in good agreement with measurement (*SI Appendix*, Fig. S6*B*). The ability to track localized tissue temperatures during both cryo- and RF ablation could provide clinicians with improved accuracy and control in targeting and ablating aberrant electrical foci, resulting in improved treatment.

In addition to temperature profiles, similar classes of webs, when firmly bonded to thin (~300 μm) soft (Young's modulus ~60 kPa) sheets of silicone (Ecoflex 0030) can spatially map mechanical strain distributions, providing critical intraprocedural insight into mechanical contractions of the heart and shifts in heart rate during sinus and arrhythmic rhythm. The key advantage of real-time strain sensing over competing imaging analysis techniques like MRI is in the intraprocedural mode of use, which enables physicians to track sudden shifts in local contractions as they occur. Technologies, ranging from metal wires to Si plates and mercury-in-rubber structures, have been used for monitoring strain in various parts of the body (46–48), but none offers the combination of characteristics needed for epicardial applications. Ultrathin Si NM (49) configured into piezoresistors as narrow strips in rosettes with longitudinal, diagonal, and transverse orientations provide a solution, incorporated into the web platform (Fig. 3 *A* and *B*, *SI Appendix*, and *SI Appendix*, Fig. S7) Information on related flexible devices appears elsewhere (50). Mounting such strain-sensing webs on ~0.3-mm-thick silicone substrates finalizes the fabrication (Fig. 3*C* and *SI Appendix*). Subjecting the substrate to uniaxial tension induces changes in resistance, as plotted in *SI Appendix*, Fig. S8 *A* and *B*. The effective gauge factor is defined as $GF = GF_{\mathrm{Si}} \times \varepsilon_g/\varepsilon_a$, where GF_{Si} = 100 is the intrinsic gauge factor of single crystalline, ε_g is the average strain in the gauge, and ε_a is the applied strain. Mechanics modeling (*SI Appendix*) gives analytically ε_g for the longitudinal gauge and therefore the effective GF is obtained as:

$$GF = GF_{\mathrm{Si}}\left[1+\frac{5(EA)_g}{\pi E_{\mathrm{silicone}}L_g^2}g_2\left(\frac{w_g}{L_g},\nu_{\mathrm{silicone}}\right)\right]^{-1}, \qquad [4]$$

where $(EA)_g$, L_g, and w_g are the tensile stiffness, length, and width of the gauge, respectively; E_{silicone} and ν_{silicone} are the Young's modulus and Poisson's ratio of the silicone; and the function g_2 is given analytically in *SI Appendix*. Using experimental data of $(EA)_g = 1.6$ N, $E_{\mathrm{silicone}} = 200$ kPa, $\nu_{\mathrm{silicone}} = 0.48$, L_g = 0.48 mm, w_g = 80 μm, Eq. **4** gives GF = 0.22, which agrees well with effective GF of 0.23 measured in experiments. This value is much smaller than GF_{Si}, as expected owing to the huge elastic mismatch between Si NM resistor and the substrate (51). The transverse gauge experiences compression due to the lateral contraction of the substrate that results from the Poisson effect; its resistance decreases. The diagonal gauge does not deform significantly; its response is, therefore, negligible. These results can be verified quantitatively by FEA in Fig. 3*D*. A silicone sheet bonded to a group of strain rosettes is stretched along direction 2 by 10%. Contour plots of longitudinal strain in direction 2 (ε_{22}) of silicone substrate and Si NMs appear in Fig. 3*D*, *Left* and *Center*. The average tensile strain in the longitudinal resistor is only 0.023% when the substrate is stretched by 10%, resulting in

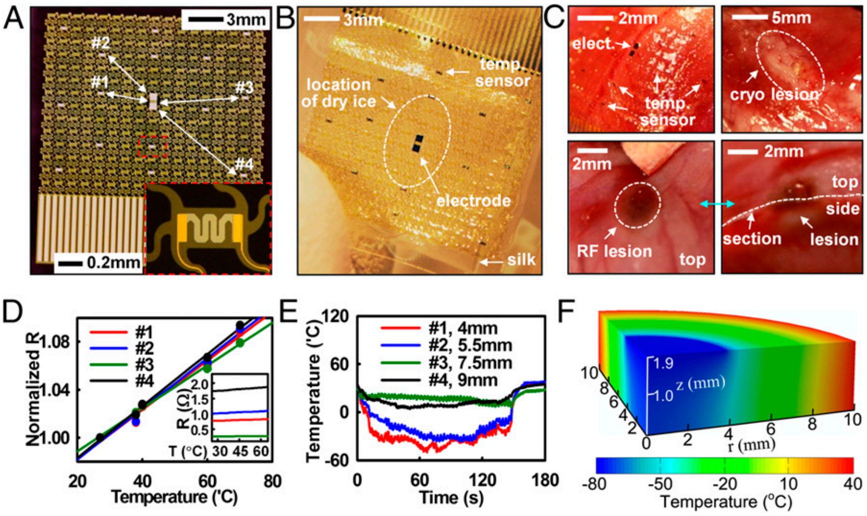

Fig. 2. Stretchable temperature sensor web to monitor cryo- and RF ablation. (*A*) Sensor web, with *Inset* of a magnified view of a temperature sensor. Four locations, denoted by #1 to #4, were monitored during cryo-ablation. (*B*) Sensor web on a silk substrate. Dry ice caused cryo-lesions when in direct contact with the epicardial surface (white dotted circle) for ~1 min. (*C*) Image of temperature sensor web on the epicardial surface (*Upper Left*) and lesions formed by cryo-ablation (*Upper Right*) and RF ablation (*Lower*). (*D*) Calibration curve for temperature sensors, showing normalized resistance at each temperature. (*Inset*) Raw temperature data. (*E*) Temperature change as a function of time during dry ice application. (*F*) Computed temperature distribution during cryo-ablation.

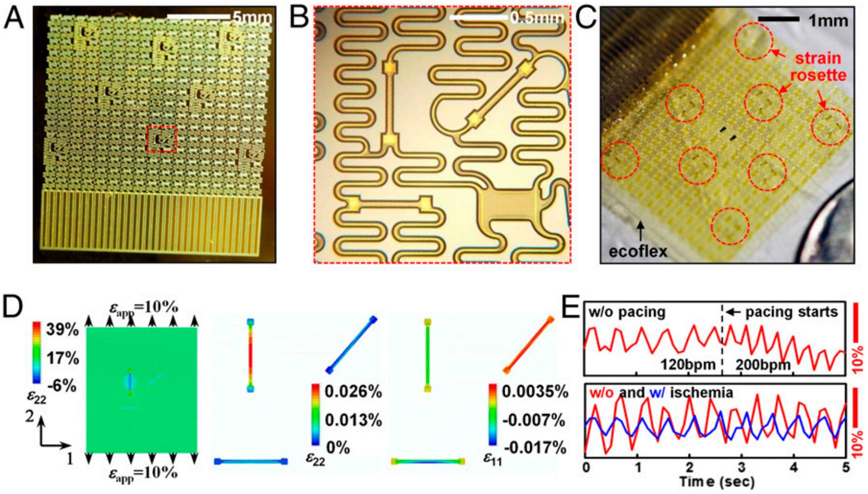

Fig. 3. Fabrication, characterization, and modeling of Si NM strain gauge webs. (*A*) Optical image of array of strain gauges on a handle wafer. (*B*) Enlarged view of the red dotted box showing one of eight strain rosettes with longitudinal, diagonal, and transverse Si NM piezoresistors. (*C*) Optical image of array of eight stretchable strain rosettes on 0.3-mm-thick silicone substrate. *(D)* Strain distribution in silicone and a Si NM, induced by 10% uniaxial tensile strain. (*Left*)The longitudinal strains (ε_{22}) in the silicone are uniformly distributed (near 10%) except for the area covered by a longitudinally oriented Si NM; (*Center*) the ε_{22} in the Si NM are three orders of magnitude smaller than the applied strain; (*Right*) the transverse strains (ε_{11}) in the transverse Si NM are negative owing to the Poisson's effect in the silicone. (*E*) In vivo test on the beating rabbit heart.

$GF = 0.23$ according to Eq. **4**. Fig. 3*D*, *Right* shows the contour plots of strains in direction 1 (ε_{11}, i.e., transverse strain) in the Si NMs. The average strain in the transverse resistor is −0.0070% after 10% longitudinal stretch, resulting in a 0.70% decrease in resistance. As shown in Fig. 3*D*, *Center* and *Right*, strains in the diagonal resistor approach zero (zero resistance change).

Applying such soft and stretchable strain gauges to a beating heart reveals strain patterns associated with expansion/contraction (Fig. 3*E*). Peak-to-peak strains were 5%∼15%, depending on the location of the devices on the heart. Systolic strains obtained in this study agree with those obtained by MRI (52) and by FEA (53). Comparing the strain results before and after pacing, we notice that pacing alters the frequency but not the amplitude. However, by comparing the strain results before and after ischemia, we see changes in both frequency and amplitude. Reduced cardiac output caused by ischemia slows down the normal rhythm and also significantly reduces the amplitude, thereby providing insight into the progression of disease states.

As a final demonstration, we illustrate tactile sensing, integrated on the surfaces of collapsible balloon catheters that undergo extreme mechanical deformations during use. For high-efficacy ablation, it is important to establish full, conformal contact with the endocardial surface to eliminate the heat sink caused by blood flow around the surface of the balloon. As a demonstration of a technology that can assess contact in the context of this need, we integrated microelectrodes on the surface of the balloon as a way to capture mechanical interactions at the balloon–tissue interface, through measurements of electrical impedance. To date, X-ray imaging has been the most widely used tool to assess contact. However, X-ray exposure has harmful health side effects, necessitating new routes to limit exposure during ablation procedures (54). Fig. 4 *A* and *B* provides images of a representative balloon catheter with impedance-based devices, positioned slightly distal to the equator (*SI Appendix*), in its inflated and deflated state (for a cardiac web deployed by catheter in a cardiac chamber, Fig. 4*C*). Alternative classes of sensors with related functionality using conductive-silicone pads were reported previously (55). Although these devices provide quantitative measures of pressure, they involve a thick, multilayer construction (∼30 μm), susceptible to mechanical damage during deployment and use. Impedance-based sensors, with simple and thin profiles (<5 μm), offer high sensitivity, fast response, and EGM mapping ability. Here, we inject small amounts (<10 μA) of alternating current across two terminals and measure voltage changes caused by differences in conductivities of surrounding media. To test this sensor concept on balloons, impedance differences between excised chicken muscle tissue and saline solution were first tested in vitro. The results show definitive shifts in impedance during on/off contacts (*SI Appendix*, Fig. S9). The same impedance-based tactile sensor array was applied to a porcine model for endocardial contact sensing in vivo. The difference in conductivity, σ, between myocardial tissue and blood (factor of ∼2–3) was sufficient to register differences. Fig. 4*C* shows X-ray images of a representative balloon in the ostium of the superior vena cava. Such images provide real-time poor visual feedback on the state and position of the balloon with respect to the ostia in the atria. Contact with cardiac tissue was detected with high levels of confidence with negligible impedance changes by inflation and deflation of the balloon (Fig. 4*D*). To measure local contact in other endocardial regions of the heart with complex anatomy, like the ventricles, requires either porous, inflatable mesh substrates with nanomembrane formats embedded on the mesh, or partially space-occupying "wands or leaf-shaped" directable, curved balloons, to facilitate blood flow inside the ventricles during operation.

Conclusions

The sensing and actuator webs described here constitute a class of cardiac medical devices suited for capturing physiological data from large areas of beating hearts without imposing significant mechanical loads or inducing any adverse effects during the course of a typical measurement. These systems are significantly softer and

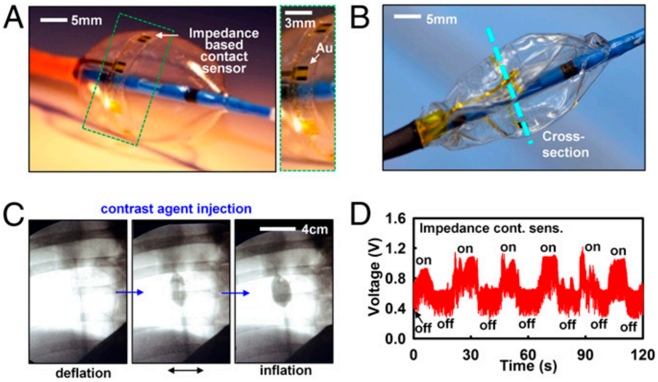

Fig. 4. Impedance-based contact sensor webs, on collapsible balloon catheters. (*A*) Optical image of a device (*Left*), with magnified view (*Right*), and picture in its deflated state (*B*). (*C*) X-ray image of balloon catheter demonstrating contact and noncontact conditions near the superior vena cava in a live porcine model. (*D*) In vivo tests impedance contact sensors. Inflation and deflation cycling experiments confirm that sudden increases in impedance coincide with the contact event.

thinner than existing devices, and because they exploit modern techniques in semiconductor device fabrication, they are immediately scalable to large areas and large numbers of multifunctional sensors, actuators, and electronics. Materials layouts and mechanics formats guide optimal design configurations that establish strong adhesion at the tissue–device interface, without separate adhesives, thereby providing attractive features for minimally invasive clinical use and for basic research in Langendorff-perfused heart models. Related web systems on catheters and other surgical tools have direct relevance to many implantable cardiac procedures.

Materials and Methods

Detailed fabrication information of EGM webs, temperature sensor and strain gauge webs, and impedance sensors on balloon catheter is shown in *SI Appendix*. Design of data acquisition system and related hardware is also described in *SI Appendix*. All animal procedures and experiments were approved by the Institutional Animal Care and Use Committee at the University of Arizona and by the Massachusetts General Hospital Center for Comparative Medicine.

ACKNOWLEDGMENTS. We thank Roja Nunna and Nishan Subedi for implementation and testing of the data acquisition system, and Behrooz Dehdashti and members of the Sarver Heart Center for help with in vivo animal studies. This material is based on work conducted at the Materials Research Laboratory and Center for Microanalysis of Materials (DE-FG02-07ER46453) at the University of Illinois at Urbana–Champaign. This work was supported by the World Class University (WCU) program through the National Research Foundation of Korea funded by the Ministry of Education, Science and Technology (R31-10013) and the Basic Science Research Program through the Korea National Research Foundation funded by Ministry of Education, Science and Technology Grant 2012R1A1A1004925. J.A.R. has received a National Security Science and Engineering Faculty Fellowship. N.L. receives support from the startup fund from the Cockrell School of Engineering at the University of Texas at Austin.

1. Calkins H, et al.; Heart Rhythm Society; European Heart Rhythm Association; European Cardiac Arrhythmia Society; American College of Cardiology; American Heart Association; Society of Thoracic Surgeons (2007) HRS/EHRA/ECAS expert consensus statement on catheter and surgical ablation of atrial fibrillation: Recommendations for personnel, policy, procedures and follow-up. *Europace* 9(6):335–379.
2. Kléber AG, Rudy Y (2004) Basic mechanisms of cardiac impulse propagation and associated arrhythmias. *Physiol Rev* 84(2):431–488.
3. Kato R, et al. (2003) Pulmonary vein anatomy in patients undergoing catheter ablation of atrial fibrillation: Lessons learned by use of magnetic resonance imaging. *Circulation* 107(15):2004–2010.
4. Aziz JNY, et al. (2009) 256-channel neural recording and delta compression microsystem with 3D electrodes. *IEEE J Solid-State Circuits* 44:995–1005.
5. Dewire J, Calkins H (2010) State-of-the-art and emerging technologies for atrial fibrillation ablation. *Nat Rev Cardiol* 7(3):129–138.
6. Viventi J, et al. (2010) A conformal, bio-interfaced class of silicon electronics for mapping cardiac electrophysiology. *Sci Transl Med* 2(24):24ra22.
7. Greenspon A (2000) Advances in catheter ablation for the treatment of cardiac arrhythmias. *IEEE Trans Microw Theory Tech* 48:2670–2675.
8. Haïssaguerre M, et al. (1998) Spontaneous initiation of atrial fibrillation by ectopic beats originating in the pulmonary veins. *N Engl J Med* 339(10):659–666.
9. Haïssaguerre M, et al. (2002) Mapping and ablation of idiopathic ventricular fibrillation. *Circulation* 106(8):962–967.
10. Dong J, Calkins H (2005) Technology insight: Catheter ablation of the pulmonary veins in the treatment of atrial fibrillation. *Nat Clin Pract Cardiovasc Med* 2(3):159–166.
11. Haïssaguerre M, et al. (2005) Catheter ablation of long-lasting persistent atrial fibrillation: Clinical outcome and mechanisms of subsequent arrhythmias. *J Cardiovasc Electrophysiol* 16(11):1138–1147.
12. Pappone C, Santinelli V (2006) Mapping and ablation: A worldwide perspective. *J Interv Card Electrophysiol* 17(3):195–198.
13. Wazni OM, et al. (2005) Radiofrequency ablation vs antiarrhythmic drugs as first-line treatment of symptomatic atrial fibrillation: A randomized trial. *JAMA* 293(21):2634–2640.
14. Ramanathan C, Ghanem RN, Jia P, Ryu K, Rudy Y (2004) Noninvasive electrocardiographic imaging for cardiac electrophysiology and arrhythmia. *Nat Med* 10(4):422–428.
15. Rudy Y (2010) Noninvasive imaging of cardiac electrophysiology and arrhythmia. *Ann N Y Acad Sci* 1188:214–221.
16. Faris OP, et al. (2003) Novel technique for cardiac electromechanical mapping with magnetic resonance imaging tagging and an epicardial electrode sock. *Ann Biomed Eng* 31(4):430–440.
17. Harrison L, et al. (1980) The sock electrode array: A tool for determining global epicardial activation during unstable arrhythmias. *Pacing Clin Electrophysiol* 3(5):531–540.
18. McVeigh E, Faris O, Ennis D, Helm P, Evans F (2002) Electromechanical mapping with MRI tagging and epicardial sock electrodes. *J Electrocardiol* 35(Suppl):61–64.
19. Sutherland DR, Ni Q, MacLeod RS, Lux RL, Punske BB (2008) Experimental measures of ventricular activation and synchrony. *Pacing Clin Electrophysiol* 31(12):1560–1570.
20. Worley SJ, et al. (1987) A new sock electrode for recording epicardial activation from the human heart: One size fits all. *Pacing Clin Electrophysiol* 10(1 Pt 1):21–31.
21. De Filippo P, He DS, Brambilla R, Gavazzi A, Cantù F (2009) Clinical experience with a single catheter for mapping and ablation of pulmonary vein ostium. *J Cardiovasc Electrophysiol* 20(4):367–373.
22. He B, Liu C, Zhang Y (2007) Three-dimensional cardiac electrical imaging from intracavity recordings. *IEEE T Bio-Med Eng* 54:1454–1460.
23. Hindricks G, Kottkamp H (2001) Simultaneous noncontact mapping of left atrium in patients with paroxysmal atrial fibrillation. *Circulation* 104(3):297–303.
24. Morgan JM, Delgado V (2009) Lead positioning for cardiac resynchronization therapy: Techniques and priorities. *Europace* 11(Suppl 5):v22–v28.
25. Narayan SM, et al. (2011) Classifying fractionated electrograms in human atrial fibrillation using monophasic action potentials and activation mapping: Evidence for localized drivers, rate acceleration, and nonlocal signal etiologies. *Heart Rhythm* 8(2):244–253.
26. Ouyang F, et al. (2005) Electrophysiological findings during ablation of persistent atrial fibrillation with electroanatomic mapping and double Lasso catheter technique. *Circulation* 112(20):3038–3048.
27. Friedman PA (2002) Novel mapping techniques for cardiac electrophysiology. *Heart* 87(6):575–582.
28. Garan H, Fallon JT, Rosenthal S, Ruskin JN (1987) Endocardial, intramural, and epicardial activation patterns during sustained monomorphic ventricular tachycardia in late canine myocardial infarction. *Circ Res* 60(6):879–896.
29. Gepstein L, Hayam G, Ben-Haim SA (1997) A novel method for nonfluoroscopic catheter-based electroanatomical mapping of the heart. In vitro and in vivo accuracy results. *Circulation* 95(6):1611–1622.
30. Packer DL (2004) Evolution of mapping and anatomic imaging of cardiac arrhythmias. *J Cardiovasc Electrophysiol* 15(7):839–854.
31. Wittig JH, Boineau JP (1975) Surgical treatment of ventricular arrhythmias using epicardial, transmural, and endocardial mapping. *Ann Thorac Surg* 20(2):117–126.
32. Kim DH, et al. (2008) Stretchable and foldable silicon integrated circuits. *Science* 320(5875):507–511.
33. Viventi J, et al. (2011) Flexible, foldable, actively multiplexed, high-density electrode array for mapping brain activity in vivo. *Nat Neurosci* 14(12):1599–1605.
34. Kim DH, et al. (2010) Dissolvable films of silk fibroin for ultrathin conformal bio-integrated electronics. *Nat Mater* 9(6):511–517.
35. Kim DH, et al. (2011) Epidermal electronics. *Science* 333(6044):838–843.
36. Latimer HB, Sawin PB (1959) Morphogenetic studies of the rabbit. XXIV. The weight and thickness of the ventricular walls in the rabbit heart. *Anat Rec* 135:141–147.
37. Jacot JG, Martin JC, Hunt DL (2010) Mechanobiology of cardiomyocyte development. *J Biomech* 43(1):93–98.
38. Michalske T, Fuller E (1985) Closure and repropagation of healed cracks in silicate glass. *J Am Ceram Soc* 68:586–590.
39. Chaudhury M, Whitesides G (1991) Direct measurement of interfacial interactions between semispherical lenses and flat sheets of poly(dimethylsiloxane) and their chemical derivatives. *Langmuir* 7:1013–1025.
40. Qian J, Gao H (2006) Scaling effects of wet adhesion in biological attachment systems. *Acta Biomater* 2(1):51–58.
41. Lu N, Yoon J, Suo Z (2007) Delamination of stiff islands patterned on stretchable substrates. *Int J Mater Res* 98:717–722.
42. Martin RW, Johnson CC (1989) Design characteristics for intravascular ultrasonic catheters. *Int J Card Imaging* 4(2-4):201–216.
43. Corbin LV, 2nd, Scher AM (1977) The canine heart as an electrocardiographic generator. Dependence on cardiac cell orientation. *Circ Res* 41(1):58–67.
44. Zhang H, et al. (2002) Determination of thermal conductivity of biomaterials in the temperature range 233–313K using a tiny detector made of a self-heated thermistor. *Cell Preserv Technol* 1:141–147.
45. Valvano J, Cochran J, Diller K (1985) Thermal-conductivity and diffusivity of biomaterials measured with self-heated thermistors. *Int J Thermophys* 6:301–311.
46. Bell G, Nielsen PE, Lassen NA, Wolfson B (1973) Indirect measurement of systolic blood pressure in the lower limb using a mercury in rubber strain gauge. *Cardiovasc Res* 7(2): 282–289.
47. Chao EY, An KN, Askew LJ, Morrey BF (1980) Electrogoniometer for the measurement of human elbow joint rotation. *J Biomech Eng* 102(4):301–310.
48. Rome K, Cowieson F (1996) A reliability study of the universal goniometer, fluid goniometer, and electrogoniometer for the measurement of ankle dorsiflexion. *Foot Ankle Int* 17(1):28–32.
49. Rogers JA, Lagally MG, Nuzzo RG (2011) Synthesis, assembly and applications of semiconductor nanomembranes. *Nature* 477(7362):45–53.
50. Won SM, et al. (2011) Piezoresistive strain sensors and multiplexed arrays using assemblies of single-crystalline silicon nanoribbons on plastic substrates. *IEEE Trans Electron Dev* 58:4074–4078.
51. Sun J, et al. (2009) Inorganic islands on a highly stretchable polyimide substrate. *J Mater Res* 24:3338–3342.
52. Haber I, Metaxas DN, Geva T, Axel L (2005) Three-dimensional systolic kinematics of the right ventricle. *Am J Physiol Heart Circ Physiol* 289(5):H1826–H1833.
53. Nazzal CM, Mulligan LJ, Criscione JC (2012) Efficient characterization of inhomogeneity in contraction strain pattern. *Biomech Model Mechanobiol* 11(5):585–593.
54. Sarabanda AV, et al. (2005) Efficacy and safety of circumferential pulmonary vein isolation using a novel cryothermal balloon ablation system. *J Am Coll Cardiol* 46(10):1902–1912.
55. Kim DH, et al. (2011) Materials for multifunctional balloon catheters with capabilities in cardiac electrophysiological mapping and ablation therapy. *Nat Mater* 10(4):316–323.

Electronic Sensor and Actuator Webs for Large-Area Complex Geometry Cardiac Mapping and Therapy

Dae-Hyeong Kim[1⊥], Roozbeh Ghaffari[2⊥], Nanshu Lu[3⊥], Shuodao Wang[4⊥], Stephen P. Lee[2], Hohyun Keum[5], Robert D'Angelo[2], Lauren Klinker[2], Yewang Su[4], Chaofeng Lu[4,6], Yun-Soung Kim[5], Abid Ameen[5], Yuhang Li[4,7], Yihui Zhang[4], Bassel de Graff[2], Yung-Yu Hsu[2], Zhuangjian Liu[8], Jeremy Ruskin[9], Lizhi Xu[5], Chi Lu[5], Fiorenzo G. Omenetto[10], Yonggang Huang[4], Moussa Mansour[9], Marvin J. Slepian[11], John A. Rogers[5*]

[1]*Center for Nanoparticle Research of Institute for Basic Science, School of Chemical and Biological Engineering, WCU Program of Chemical Convergence for Energy and Environment, Seoul National University, Seoul 151-742, Republic of Korea*

[2]*MC10 Inc., 36 Cameron Avenue, Cambridge, MA 02140 USA*

[3]*Department of Aerospace Engineering and Engineering Mechanics, University of Texas at Austin, Austin, TX 78712, USA*

[4]*Department of Mechanical Engineering and Department of Civil and Environmental Engineering, Northwestern University, Evanston, IL 60208*

[5]*Department of Materials Science and Engineering, Beckman Institute for Advanced Science and Technology, and Frederick Seitz Materials Research Laboratory, University of Illinois at Urbana-Champaign, Urbana, IL 61801 USA*

[6]*Soft Matter Research Center & Department of Civil Engineering, Zhejiang University, Hangzhou 310058, China*

[7]*School of Astronautics, Harbin Institute of Technology, Harbin 150001, China*

[8]*Institute of High Performance Computing, 1 Fusionopolis Way, #16-16 Connexis, Singapore 138632.*

[9]*Massachusetts General Hospital, Cardiac Arrhythmia Unit, Boston, MA. 02140 USA*

[10]*Department of Biomedical Engineering, Tufts University, Medford, MA. 02155 USA*

[11]*Sarver Heart Center, University of Arizona, Tucson, AZ 85724 USA*

[⊥]*These authors contributed equally.*

*To whom correspondence should be addressed. E-mail: jrogers@illinois.edu

Supporting Information

1. SI Materials and Methods

Fabrication of the EGM webs

The fabrication starts with spin coating of polyimide (PI, ~1.2 µm, Sigma Aldrich, USA) onto a film of poly(methylmethacrylate) (PMMA, 100 nm, MicroChem, USA) cast on a silicon wafer. Electron beam evaporation forms an adhesion layer and metallization for island and interconnects (Cr/Au, 5 nm/150 nm), defined into appropriate patterns by photolithography and etching. A second, top layer of PI (~1.2 µm) insulates the system and places the metal near the neutral mechanical plane in the PI/metal/PI stack. The open web design results from etching through the entire thickness of this trilayer with oxygen reactive ion etching (RIE) in a pattern defined by photolithography. The final device appears in Fig. 1*A*. The total number of paired electrodes is 17. Dissolving the silk substrate releases a free-standing web that is transfer printed to a silk substrate, and then connected to an anisotropic conductive film (ACF) for interfacing to a data acquisition system, thereby completing the fabrication.

Fabrication of temperature sensor and strain gauge webs

The designs and fabrication procedures are similar to those described above. The temperature sensing web uses platinum resistors at the locations of the islands. Here, thin layers of Ti/Pt (5 nm/50 nm) deposited by electron beam evaporation and patterned by photolithography and then lift-off defines the sensors. Surface treatment of the PI with UV/Ozone or deposition of a thin silicon dioxide (SiO_2) layer (~50 nm) on top of PI improves the adhesion of the Ti/Pt. Fabrication of strain gauge rosettes relies on transfer printing of boron-doped (doping concentration $\sim 5 \times 10^{18}$ /cm^3), 340nm-thick silicon resistors onto the island regions. Both sensors use serpentine interconnects of Cr/Au. Additional encapsulation with PI prevents electrical leakage currents, and places the components near the neutral mechanical plane. A final device appears in Fig. 1*A*. Transfer printing the mesh to silk and establishing ACF connections completes the process. The temperature sensor and strain gauge arrays contain 16 and 8 paired nodes, respectively. Detailed designs of temperature sensor and strain gauge array appear in Fig. S3 and S7, respectively.

Fabrication of impedance contact sensor webs and integration on collapsible balloon catheters

The fabrication process is identical to the stretchable electrode array processing, but with the addition of an encapsulating layer of polymer (Dymax Inc.) for planarization (Fig. S10). Flexible printed circuit boards connect to the sensor arrays using anisotropic conductive epoxy, applied with heat (175° C) and pressure. Thin-walled heat shrink tubing insulates the ribbons and wires, to provide water-proof encapsulation.

Impedance-based contact, temperature and strain gauge data acquisition design

The data acquisition system consists of three modules to measure impedance-based contact, temperature and strain (Fig. S11). A MMBT4403 PNP transistor is placed in the feedback path of the AD8671 operational amplifier to create a voltage-controlled current source. For contact sensing, the excitation current from the current source passes through tissue to generate a voltage, which is then measured with a National Instruments PXI-6289 data acquisition card. Custom LabView software was written to control the output current and frequency of the excitation current. The excitation currents were set <10 µA and measurements were collected at 1 kHz and 10 kHz. For temperature and strain gauge recordings, two custom, multi-channel software-controlled current sources operate the web arrays. A PXI-6289, controlled with custom LabView software, controls voltages across either sensor type. The excitation consisted of a DC current between 50 µA to 1 mA.

Electrophysiological signal data acquisition design

The electrophysiological signals detected by the web arrays were conditioned with an Intan RHA1016 multiplexed biopotential amplifier. A digital signal processing system (Grapevine system, Ripple Inc) converted the multiplexed analog signal from the RHA1016 to digital output. The RHA1016's output was sampled at 300 ksps and decimated at 1 ksps for individual channels. In addition, the Grapevine system applied a digital 50/60 Hz notch filter to the signal. The data are recorded in the Cyberkinetics NEV2.2 NS2 format and viewed with custom Matlab software.

Animal preparations

Experiments used rabbit models (n = 5; 3.5-4.0 kg), anaesthetized with a 0.5 ml/kg mixture of ketamine (30 mg/kg), xylazine (7 mg/kg) and acepromazine (3:5 mg/kg), and then intubated and maintained with 2% isoflurane at room temperature. Access to the epicardial surface is enabled by sternotomy and pericardiotomy. Once exposed, sensor webs placed in direct contact with the anterior surface of the ventricles provides the measurement modality. Ringer's solution maintains a moist epicardial surface during experiments. Measurements made at multiple sites along RV and LV surfaces allow differentiation of local excitation across the different chambers of the heart during normal and following ischaemic-injury.

Porcine models (n = 3; 80-100 kg) were anesthetized. Heart rate monitoring electrodes, EGM, respiratory rate, intravenous blood pressure monitor and a periodic toe pinch to test for pedal withdrawal provided assessment of anesthetic depth. Lactated Ringer’s solution was administered via IV at a rate of 10 mL/kg/hr (Saline 0.9% solution 10mL/kg/hr can be substituted). Jugular and femoral venous access were achieved by shaving the skin around these areas to facilitate access in the veins. The guide-wires, cardiac sheaths, were deployed via the femoral vein. Contrast dye was injected into the balloon and x-ray images were captured to determine the position of the balloon during inflation cycles. The Institutional Animal Care and Use Committee at the University of Arizona approved of all experiments.

2. Detailed information of the electrical system and temperature sensor

The size of one electrode (see Fig. S1) is 560 μm × 290 μm and the center to center distance between electrodes in one differential pair is 1 mm. When films of chromium (5 nm; adhesion promoter) / gold (150 nm), deposited by electron beam evaporation and photolithographically patterned into pads with dimensions of 250 μm × 250 μm are used, the impedance is ~84 kOhm (measured in saline solution using the integrated device structure, with interconnects and the sensing electrode exposed). Typically the electrical impedance reduces to ~29 kOhm with the addition of a bilayer titanium (5 nm; adhesion promoter) / platinum (50 nm) on top of the same chromium / gold electrode. The signal to noise ratios estimated directly from recorded EGM signals measured when mounted on the epicardial surface are typically greater than 40 (with gold electrodes). The center-to-center distance between each electrode pair is more than ~3 mm, which is sufficiently large to minimize cross-talk. The entire electrode array in the current design measures ~16 mm × ~14 mm and can cover the exposed surfaces of hearts in small animal models. Straightforward scaling of the same fabrication schemes, materials and mechanics designs can enable analogous devices for the human heart. One of the advantages of cardiac web design is, as described in the frictional analysis, that it minimizes effects of sliding, thereby suppressing motion artifacts. The criterion for acceptable leakage current was less than ~10 μA, typically less than ~1 μA.

Precision hot plates were used to establish calibration curves for the temperature sensors. After establishing conformal contact of a sensor to the center of the hot plate, the resistance change was measured as a function of temperature. The time response associated with changes in resistance is less than a second. The normalized (resistance of each measurement divided by the resistance at the initial temperature) calibration results and non-normalized, raw results appear in Fig. 2*D* and its inset. The resistance varies linearly with temperature, as expected. Depending on the detection electronics, the precision of the temperature measurement can be as high as ~0.02°C.

3. Tensile and Bending stiffness of mapping electrode arrays

The electrode arrays (Fig. 1*A*) consist of electrode islands of widths w_x and w_y, double serpentine interconnects along the *y*- direction (Figs. S2*A* and *C*) and single serpentine interconnects along the *x*-direction (Fig. S2*B*) with arc radii *r* and *R* and width *b*. The interconnects are much more compliant than the electrode islands such that they deform to accommodate all stretching and/or bending. The tensile and bending stiffness of mapping electrode arrays, with and without the silk substrate, are obtained analytically in the following.

For an interconnect subjected to a pair of forces *F* at both ends, the bending moment *M* in the interconnect is obtained in terms of coordinates of the center of cross location, and is linearly proportional to *F*. The strain energy is dominated by the bending energy, which is given by $U \approx U_{\text{bending}} = \int M^2 ds \Big/ \left(2\overline{EI}_{z,\text{int}} \right)$, where $\overline{EI}_{z,\text{int}}$ is the in-plane bending stiffness of the interconnect, and the integration is along the arc length *s* of the interconnect. The elongation of each interconnect is $u = \partial U / \partial F$, which is linearly proportional to *F*. The effective tensile stiffness of the electrode arrays without the silk substrate is

$$\begin{cases} \overline{EA}_x = \dfrac{F\left(w_x + L_{bx}\right)}{u\left(w_y + L_{by}\right)} \\ \overline{EA}_y = \dfrac{2F\left(w_y + L_{by}\right)}{u\left(w_x + L_{bx}\right)} \end{cases}, \tag{S1}$$

where $L_{\mathrm{by}}=2R+8r$ and $L_{\mathrm{bx}}=2R+4r$ are bridge lengths along y- and x- directions in Figs. S2*A* and S2*B*, respectively. Equation (S1) can also be written analytically as

$$\begin{cases} \overline{EA}_x = \dfrac{\overline{EI}_{z,\mathrm{int}}\left(w_x + 2R + 4r\right)}{2R^3\left(w_y + 2R + 8r\right)} \left\{ \begin{array}{l} \dfrac{3}{4}\pi - \dfrac{5}{3} + \pi\eta + 4\eta^2 + \dfrac{\pi}{2}\eta^3 \\ -\dfrac{\left[\pi - 3 + 2(\pi-2)\eta + 2\pi\eta^2 + 4\eta^3\right]^2}{3\pi - 8 + 8(\pi-2)\eta + 8\pi\eta^2 + 6\pi\eta^3} \end{array} \right\}^{-1} \\ \overline{EA}_y = \dfrac{\overline{EI}_{z,\mathrm{int}}\left(w_y + 2R + 8r\right)}{R^3\left(w_x + 2R + 4r\right)} \left\{ \begin{array}{l} \dfrac{3}{4}\pi - 1 + 2\pi\eta + 8\eta^2 + \pi\eta^3 \\ -\dfrac{(1+2\eta)^2\left[\pi - 3 + 2(\pi-1)\eta + 4\eta^2\right]^2}{3\pi - 8 + 16(\pi-2)\eta + 32(\pi+1)\eta^2 + 44\pi\eta^3} \end{array} \right\}^{-1} \end{cases}, \tag{S2}$$

where $\eta=r/R$. The tensile stiffness of electrode arrays with the silk substrate is given by

$$\begin{cases} \overline{EA}_{x\text{-silk}} = \overline{EA}_x + \overline{E}_{\mathrm{silk}} h_{\mathrm{silk}} \\ \overline{EA}_{y\text{-silk}} = \overline{EA}_y + \overline{E}_{\mathrm{silk}} h_{\mathrm{silk}} \end{cases}, \tag{S3}$$

where $\overline{E}_{\mathrm{silk}}$ and h_{silk} are the elastic modulus and thickness of silk substrate, respectively.

For an interconnect subjected to a pair of out-of-plane bending moments M_0 at both ends, the bending moments in the normal direction M_n, out-of-plane direction M_z and torque T_s in the interconnect is obtained in terms of the orientation of the cross section, and is linearly proportional to M_0. The strain energy is dominated by the bending and torsion energies, and is given by $U \approx U_{\text{bending-}n} + U_{\text{bending-z}} + U_{\text{torsion}} = \int M_n^2 ds \Big/ \left(2\overline{EI}_{n,\mathrm{int}}\right) + \int M_z^2 ds \Big/ \left(2\overline{EI}_{z,\mathrm{int}}\right) + \int T_s^2 ds \Big/ \left(2\overline{GJ}_s\right)$, where $\overline{EI}_{n,\text{int}}$ is the bending stiffness in the *n*-direction (Figs. S2*A* and S2*B*), and $\overline{GJ}_s$ is the torsion stiffness of the interconnect. The relative rotation between two ends of the interconnect is $\theta_0 = \partial U / \partial M_0$, which is linearly proportional to M_0. The effective bending stiffness of the electrode arrays without the silk substrate is

$$\begin{cases} \overline{EI}_x = \dfrac{M_0\left(w_x + L_{bx}\right)}{\theta_0\left(w_y + L_{by}\right)} \\ \overline{EI}_y = \dfrac{2M_0\left(w_y + L_{by}\right)}{\theta_0\left(w_x + L_{bx}\right)} \end{cases}, \tag{S4}$$

or

$$\begin{cases} \overline{EI}_x = \dfrac{2\overline{GJ}_s\left(w_x + 2R + 4r\right)}{R\left(w_y + 2R + 8r\right)} \left[\begin{array}{c} 4 + \pi + 2\pi\eta + \pi\beta\left(1 + 2\eta\right) \\ -\dfrac{4\left(\beta - 1\right)^2}{\beta\left(4 + \pi + 2\pi\eta\right) + \pi\left(1 + 2\eta\right)} \end{array} \right]^{-1} \\ \overline{EI}_y = \dfrac{4\overline{GJ}_s\left(w_y + 2R + 8r\right)}{R\left(w_x + 2R + 4r\right)} \left[\begin{array}{c} 12 + \pi + 4\pi\eta + \pi\beta\left(1 + 4\eta\right) \\ -\dfrac{4\left(\beta - 1\right)^2}{\beta\left(12 + \pi + 4\pi\eta\right) + \pi\left(1 + 4\eta\right)} \end{array} \right]^{-1} \end{cases}, \tag{S5}$$

where $\beta = \overline{GJ}_s / \overline{EI}_{n,\text{int}}$. The bending stiffness of the electrode arrays with the silk substrate can be similarly obtained following the approach by Kim *et al.* (1) and Wang *et al.* (2). These analytical expressions of the tensile and bending stiffness agree very well with FEA, as shown in the Table S1 and 2.

The stiffness along the *x* and *y* directions are, in fact, quite similar such that only their average values are reported in the paper. The analysis above does not account for buckling of the interconnects, which would result in even smaller tensile/bending stiffness such that the electrode arrays in experiments may be more compliant than the above results.

4. Coupling between the electrode array and the epicardial surface

The total potential energy $U_{\text{non-couple}}=0$ when the electrode array has no contact with the epicardial surface and remains flat. Once the electrode array conforms to the epicardial surface, the total energy U_{couple} consists of the elastic energy $U_{\text{elastic}} = U_{\text{bending}} + U_{\text{membrane}} = L^2 \overline{EI}_{\text{mesh}} \big/ R_{\text{heart}}^2 + \pi \overline{EA}_{\text{mesh}} \int_0^{L/\sqrt{\pi}} \left[1 - R_{\text{heart}} \sin\left(r/R_{\text{heart}}\right)/r\right] r dr$ and the adhesive energy of the interface $U_{\text{adhesive}} = -\gamma A$. Intimate coupling between the electrode array and the epicardial surface requires $U_{\text{couple}} = U_{\text{elastic}} + U_{\text{adhesive}} < U_{\text{non-couple}} = 0$, which leads to Eq. (1).

The interfacial bonding between rigid ribbons and a deforming substrate (the expanding/contracting heart in this case) is well studied by Lu et al. (3) who give the energy release rate for stiff ribbons on compliant substrate ($E_{\text{heart}} << E_{\text{device}}$) analytically as $G_{\text{ribbon}} = \frac{E_{\text{heart}} \varepsilon^2 L_{\text{unit}}}{8} \tan \frac{\pi w_x}{2 L_{\text{unit}}}$. In the current study, however, only part of the area (w_y/L_{unit}) is bonded to the electrode islands, and therefore the energy release rate is multiplied by this area ratio and given approximately as Eq. (2) in the text.

5. Equilibrium between the electrode island, the interconnects and the epicardial tissue

Let F_x and F_y denote the forces acting on an electrode island along the *x*- and *y*-directions (Fig. S2*F*, grey rectangular denotes the island; red substrate denotes the heart, modelled as a semi-infinite body, with *z*-direction pointing into the heart), respectively. The forces F_x and F_y are uniformly distributed over the area of the island $w_x \times w_y$. As a result, the displacements of the island at point *O* under these forces are derived from the Mindlin solution as (4)

$$\begin{aligned}\Delta_{\text{island}-x} &= \frac{1+\nu}{\pi E_{\text{heart}}}\frac{F_x}{w_x w_y}\int_{-w_y/2}^{w_y/2}\int_{-w_x/2}^{w_x/2}\left[\frac{1-\nu}{\sqrt{X^2+Y^2}}+\frac{\nu X^2}{\left(X^2+Y^2\right)^{3/2}}\right]dXdY \\ &= \frac{(1+\nu)F_x}{\pi w_x E_{\text{heart}}}\left[\ln\left(\frac{\sqrt{1+a^2}+1}{\sqrt{1+a^2}-1}\right)+\frac{1-\nu}{a}\ln\left(\frac{\sqrt{1+a^2}+a}{\sqrt{1+a^2}-a}\right)\right]\end{aligned} \tag{S6}$$

and

$$\begin{aligned}\Delta_{\text{island}-y} &= \frac{1+\nu}{\pi E_{\text{heart}}}\frac{F_y}{w_x w_y}\int_{-w_y/2}^{w_y/2}\int_{-w_x/2}^{w_x/2}\left[\frac{1-\nu}{\sqrt{X^2+Y^2}}+\frac{\nu Y^2}{\left(X^2+Y^2\right)^{3/2}}\right]dXdY \\ &= \frac{(1+\nu)F_y}{\pi w_y E_{\text{heart}}}\left[\ln\left(\frac{\sqrt{1+a^2}+a}{\sqrt{1+a^2}-a}\right)+(1-\nu)a\ln\left(\frac{\sqrt{1+a^2}+1}{\sqrt{1+a^2}-1}\right)\right]\end{aligned} \tag{S7}$$

in the *x*- and *y*- directions, respectively, where $a=w_y/w_x$. The interconnects are subjected to the same forces and therefore elongate. The elongations of the interconnects are

$$\Delta_{\text{int}-x} = \frac{F_x}{\overline{EA}_{\text{mesh}}} \tag{S8}$$

in the x-direction and

$$\Delta_{\text{int}-y} = \frac{F_y}{\overline{EA}_{\text{mesh}}} \tag{S9}$$

in the y-direction. If there is no slippage between the islands and the heart, then

$$\Delta_{\text{island}-x} + \Delta_{\text{int}-x} = \Delta_{\text{island}-y} + \Delta_{\text{int}-y} = \varepsilon L_{\text{unit}} \,. \tag{S10}$$

The total pulling force at each electrode island is $F_{\text{pull}} = \sqrt{F_x^2 + F_y^2}$. Substituting Eq. (S6-S10) into the above expression yields $F_{\text{pull}} = \overline{EA}_{\text{mesh}} \varepsilon L_{\text{unit}} g_1 \left(\frac{\overline{EA}_{\text{mesh}}}{E_{\text{heart}} w_x}, \frac{w_y}{w_x}, \frac{w_x}{L_{\text{unit}}}, \nu \right)$, where

$$g_1 = \sqrt{\begin{array}{l} \left\{ 1 + \dfrac{(1+\nu)\overline{EA}_{\text{mesh}}}{\pi w_x E_{\text{heart}}} \Bigg[\ln\left(\dfrac{\sqrt{1+a^2}+1}{\sqrt{1+a^2}-1} \right) + \dfrac{1-\nu}{a} \ln\left(\dfrac{\sqrt{1+a^2}+a}{\sqrt{1+a^2}-a} \right) \Bigg]\Bigg] \right\}^{-2} \\ + \left\{ 1 + \dfrac{(1+\nu)\overline{EA}_{\text{mesh}}}{\pi w_y E_{\text{heart}}} \Bigg[\ln\left(\dfrac{\sqrt{1+a^2}+a}{\sqrt{1+a^2}-a} \right) + (1-\nu) a \ln\left(\dfrac{\sqrt{1+a^2}+1}{\sqrt{1+a^2}-1} \right) \Bigg]\Bigg] \right\}^{-2} \end{array}} \,. \tag{S11}$$

6. Friction coefficient between the electrode array and the epicardial tissue

Patronik *et al.* (5) reported a frictional force of f~3 N in studies of epicardial surface on which a small robot was mounted over an area of A~35 mm^2 by suction at vacuum pressure of p~53 kPa. The friction coefficient is thus obtained as $\mu = f/(pA) \sim 1.6$. Other friction studies have reported smaller friction coefficient (e.g., 0.04~0.2 (6)), but even for the friction coefficient to be an order of magnitude smaller, Eq.

(3) still holds such that the electrode array does not slide because buckling of interconnects gives much smaller pulling force on the electrode island.

7. Thermal analysis of heart during cryoablation

For cryoablation to a specific region in the heart, the heat conduction equation for the temperature T is

$$k\nabla^2 T = \frac{k}{\alpha}\frac{\partial T}{\partial t}, \tag{S17}$$

where k and α are the thermal conductivity and diffusivity of heart tissue, respectively, and t is time. The ventricular wall of the heart is modeled as a slab of thickness $h = 1.9\,\text{mm}$, with the initial temperature 37 $^{\text{o}}$C (body temperature). The dry ice is approximately a cylinder with radius ~ 3.5 mm and much larger height. The outer surface of the ventricular wall in contact with the dry ice and the air temperature around the dry ice are the sublimation temperature -79 $^{\text{o}}$C of dry ice (7), which governs the natural heat convection with the outer surface of the ventricular wall. The inner surface of the ventricular wall has heat convection with the blood of constant temperature 37 $^{\text{o}}$C, but the convection coefficient is low when the ventricular wall contacts the dry ice (and therefore low temperature and slow blood flow (8)). Once the dry ice is removed, the outer surface of the ventricular wall has natural heat convection with the room-temperature air. The inner surface has heat convection with the blood flow at constant temperature of 37 $^{\text{o}}$C, though the convection coefficient increases substantially (8) for relatively fast blood flow.

The heat conduction equation is solved numerically. Its spatial and temporal distributions are shown in Figs. 2*F* and S5*B*, respectively, and the latter agrees well with experiments.

8. Thermal analysis of heart during RF ablation

For RF ablation of a specific region in the heart, the heat conduction equation is

$$k\nabla^2 T + q = \frac{k}{\alpha}\frac{\partial T}{\partial t}, \tag{S18}$$

where q is the body heat flux due to Joule heat from the electrode, and is given by $q = \sigma\nabla\phi\cdot\nabla\phi$; σ is the electrical conductivity, and the electric potential ϕ is determined from the Maxwell equation $\nabla^2\phi = 0$ (9). The heart is modeled as a disk of radius 10 mm and thickness $h = 10\ \mathrm{mm}$. The top surface of the heart has the boundary conditions $\phi = \phi_0$ and $-\sigma\frac{\partial\phi}{\partial z} = 0$ in and out of the region of electrode contact, respectively, where ϕ_0 is the prescribed voltage. The bottom surface has the boundary condition $\phi = 0$. The electric potential is obtained analytically as

$$\phi = \frac{2\phi_0}{\pi}\int_0^\infty \frac{\sinh\left[\xi(h-z)\right]}{\xi\sinh(\xi h)}\sin(\xi R_0)J_0(\xi r)\,\mathrm{d}\xi, \tag{S19}$$

where R_0 is the radius of electrode contact. The temperature field, when the electrode contacts the heart, is then obtained analytically as

$$T = T_\infty + \sigma\int_0^\infty\int_0^h \nabla\phi(r',z')\cdot\nabla\phi(r',z')G(r,z|r',z';t)\,\mathrm{d}r'\mathrm{d}z', \tag{S20}$$

where

$$G\left(r,z\middle|r',z';t\right)=\frac{2\alpha}{kh}\sum_{n=0}^{\infty}\cos\left(\frac{n\pi z}{h}\right)\cos\left(\frac{n\pi z'}{h}\right)\int_{0}^{\infty}\frac{J_0\left(\xi r'\right)r'}{\kappa_{2n}}\left(1-\mathrm{e}^{-\kappa_{2n}t}\right)J_0\left(\xi r\right)\xi\mathrm{d}\xi \quad \text{(S21)}$$

and $\kappa_{2n}=\alpha\left(\xi^2+\frac{n^2\pi^2}{h^2}\right)$, and J_0 is zeroth order Bessel function of the first kind. The temperature is also obtained analytically after the electrode is removed.

Figure S6*A* shows the temperature variation at r =4 mm obtained by the numerical method, which agrees well with the experimental results of the #2 sensor. The spatial distribution of the temperature in Fig. S6*B*, at the time $t_0=33\,\mathrm{s}$ when the probe is removed, suggests the lesion size ~4.4 mm, and lesion depth ~3.7 mm for a critical lesion temperature of ~70 $^{\circ}$C.

9. Mechanics of the strain gauge

The strain in the gauge is obtained analytically by superposition method depicted in Fig. S12*A*. The strain in the middle frame of Fig. S12*A* is $\varepsilon_1=\varepsilon_a$, and the strain in the bottom frame of Fig. S12*A* could be solved by assuming interfacial shear stress distribution of $\tau=kx^3$ at the bottom of the gauge ($-kx^3$ on the top of the substrate) as shown in Fig. S12*B*. The gauge is modelled as a beam with cross section (surface normal in the x-direction) of Fig. S12*C*. The displacement of the gauge is solved by the equilibrium of the beam. The substrate is modelled as a semi-infinite space because its thickness is ~100 times larger than that of the gauge. The displacement of the substrate (silicone) at ($x=L_g/2$, $y=z=0$), is obtained by integration of the Mindlin solution for a point force over the interface of $w_{\mathrm{g}}\times L_{\mathrm{g}}$, i.e.

$$
\begin{aligned}
u_{\mathrm{sub}} &= -\frac{1+\nu_{\mathrm{silicone}}}{\pi E_{\mathrm{silicone}}}\int_{-w_{\mathrm{g}}/2}^{w_{\mathrm{g}}/2}\int_{-L_{\mathrm{g}}/2}^{L_{\mathrm{g}}/2}\left\{\frac{1-\nu}{\sqrt{\left(\frac{L_{\mathrm{g}}}{2}-X\right)^2+Y^2}}+\frac{\nu\left(\frac{L_{\mathrm{g}}}{2}-X\right)^2}{\left[\left(\frac{L_{\mathrm{g}}}{2}-X\right)^2+Y^2\right]^{3/2}}\right\}kX^3\,dXdY \qquad ,\text{(S12)}\\
&= \frac{-kL_{\mathrm{g}}^3 w_{\mathrm{g}}}{32\pi E_{\mathrm{silicone}}}\,g_2\left(\frac{w_{\mathrm{g}}}{L_{\mathrm{g}}},\nu_{\mathrm{silicone}}\right)
\end{aligned}
$$

where

$$
\begin{aligned}
g_2 = {} & 2\left(1+\nu_{\mathrm{silicone}}\right)\left[2-\left(1+2\nu_{\mathrm{silicone}}\right)\frac{w_{\mathrm{g}}^2}{L_{\mathrm{g}}^2}\right]\ln\left(\frac{\sqrt{L_{\mathrm{g}}^2+w_{\mathrm{g}}^2}+2L_{\mathrm{g}}}{w_{\mathrm{g}}}\right)\\
& -2\left(1+\nu_{\mathrm{silicone}}\right)\left(3+5\nu_{\mathrm{silicone}}\right)\sqrt{4+\frac{w_{\mathrm{g}}^2}{L_{\mathrm{g}}^2}} \qquad . \qquad \text{(S13)}\\
& -\frac{2}{3}\left(1+\nu_{\mathrm{silicone}}\right)\left(1+3\nu_{\mathrm{silicone}}\right)\left[\frac{w_{\mathrm{g}}^3}{L_{\mathrm{g}}^3}-\left(\sqrt{4+\frac{w_{\mathrm{g}}^2}{L_{\mathrm{g}}^2}}\right)^3\right]+\frac{6w_{\mathrm{g}}}{L_{\mathrm{g}}}\left(1+\nu_{\mathrm{silicone}}\right)^2
\end{aligned}
$$

Compatibility requires the u_{sub} equal to the shortening of the gauge, which gives k analytically, and therefore the strain in the gauge ε_2. The strain on the top frame of Fig. S12*A* is $\varepsilon=\varepsilon_1+\varepsilon_2$, and its average over the length L_{g}, $\left(1/L_{\mathrm{g}}\right)\int_{-L_{\mathrm{g}}/2}^{L_{\mathrm{g}}/2}\varepsilon\,dx$, is obtained analytically as

$$
\varepsilon_{\mathrm{g}} = \frac{\varepsilon_a}{1+\frac{5\left(EA\right)_{\mathrm{g}}}{\pi E_{\mathrm{silicone}}L_{\mathrm{g}}^2}\,g_2\left(\frac{w_{\mathrm{g}}}{L_{\mathrm{g}}},\nu_{\mathrm{silicone}}\right)}. \qquad \text{(S14)}
$$

The effective gauge factor is then given as Eq. (4) in the text.

The same idea is applied to calculate the energy release rate between the silicone substrate and the tissue (e.g. chicken breast, epicardial surface). Since the small, stiff gauges do not alter the mechanical behavior of the silicone (see text), the total energy U_{tot} of the system consists of the membrane energy of the silicone and the elastic energy of the tissue, and is obtained analytically as:

$$U_{\text{tot}} = \frac{\varepsilon_{\text{a}}^2 (EA)_{\text{silicone}} L}{1 + \frac{5(EA)_{\text{silicone}}}{\pi E_{\text{tissue}} L^2} g_2\left(\frac{w_{\text{silicone}}}{L}, \nu_{\text{tissue}}\right)} \left[1 - \frac{10}{9} \frac{1}{1 + \frac{5(EA)_{\text{silicone}}}{\pi E_{\text{tissue}} L^2} g_2\left(\frac{w_{\text{silicone}}}{L}, \nu_{\text{tissue}}\right)}\right]. \text{(S15)}$$

where $(EA)_{\text{silicone}}$ and w_{silicone} are the tensile stiffness and width of the silicone, respectively; E_{tissue} and ν_{tissue} are the Young's modulus and Poisson's ratio of the tissue, respectively; L=L_{silicone}-2c is the bonded length between the silicone and the tissue, with L_{silicone} being the total length of the silicone and c the assumed crack length at the edge of the silicone. And the energy release rate is given by $G = -(1/2)(\partial U_{\text{tot}}/\partial c)\big|_{L=L_{\text{silicone}}} = (\partial U_{\text{tot}}/\partial L)\big|_{L=L_{\text{silicone}}}$. Using experimental data of ε_{a}=20%, $(EA)_{\text{silicone}}$=0.42 N, L_{silicone}=14 mm, w_{silicone}=7.0 mm, ν_{tissue}~0.45, E_{tissue}=40 kPa, this model gives G=8.0 mN/m which is ~250 times smaller than the interfacial work of adhesion between the two layers (~0.2 N/m,). To validate surface adhesion, we performed *in vitro* tests by laminating the silicone-supported stretchable strain gauges on the surface of a chicken breast, as shown in the left frame of Fig. S13*A*. When the chicken breast is stretched uniaxially by 20%, Fig. S13*B* right frame shows the gauge factor measured in this condition (0.25) is almost the same as that measured on a freestanding gauge (0.23), indicating that deformation in the chicken breast is indeed fully transferred to the soft gauge through interfacial shear stress. Figure S13*C* confirms that there is no sliding between the tissue and the gauge even after the chicken breast is stretched beyond its failure strain (20%). This observation is consistent with the above modelling results which show the energy release rate being much smaller than the interfacial work of adhesion.

FEA results (Fig. S12*D*) also indicate that the gauge only reduces the strain in a thin layer (~20% of the substrate thickness) of the silicone substrate underneath it; the strain averaged throughout the depth of the silicone in this region is 8.0% for an applied strain of 10%. Therefore, the huge elastic mismatch between the silicon NM resistor and the substrate does not alter the overall mechanical behavior of the silicone substrate, which is acting as a strain isolation layer between the tissue and the stiff silicon NM (50, 51). The devices exhibit highly reproducible behavior under cyclical loads with strains of ~30% (Fig. S8*B*). We note that bending deformations can also affect the response, as quantified by measuring the response due to wrapped around cylinders with various radii (Fig. S13*A*).

10. Mechanical stress on webs during balloon inflation/deflation cycles

The web designs minimize strains in the sensory elements of balloon systems, and thereby enhance durability during inflation and deflation of the balloon support. Compressive strains in the circuits reach maximum levels when the balloon is totally deflated. At this stage, the balloon folds into uniform ‘clover’ patterns (cross-section of

Fig. 4*B* and Fig. S14, left) driven by the pressure mismatch inside (~vacuum) and outside of the balloon (p_{air} ~1 atm). The deformed profile of each clover-fold can be obtained analytically, and verified using FEA (Fig. S14, right). The maximum curvature occurs at the peaks of the folds, and is given by $\kappa_{\max} = 2.1\left(p_{\mathrm{air}} / \overline{EI}_{\mathrm{balloon}}\right)^{1/3}$, where $\overline{EI}_{\mathrm{balloon}}$ is the bending stiffness of the balloon with circuits. The strain in the circuits/balloon membrane is then obtained as

$$\varepsilon_{\max} = \kappa_{\max} y, \tag{S16}$$

where *y* is the distance from the neutral mechanical plane (Fig. S10). This result gives the maximum strain 0.31% in gold and 1.7% in polyimide, which are much smaller than the strains 28.7% in the adhesive (encapsulation) and 39.5% polyurethane (balloon membrane) layers. The compliant photo-curable adhesive (Dymax Inc.) and polyurethane accommodate large deformation resulting from deflation, such that the strains in active components are small. The minimal curvature regions (κ=0, Fig. S14, right) undergo minimal deformation during deflation, and therefore represent the optimal locations for selective positioning of devices. These modeling results also represent a framework for integrating conformal sensors on various classes of collapsible balloons, beyond those described in this study.

SI References

1. Kim D, *et al* (2011) Epidermal electronics. *Science* 333: 838-843.

2. Wang S*, et al* (2011) Mechanics of epidermal electronics. *J Appl Mech* 79:3, article 031022.

3. Lu N, Yoon J & Suo Z (2007) Delamination of stiff islands patterned on stretchable substrates. *Int J Mater Res* 98: 717-722.

4. Barber JR (2010) in *Elasticity* (Springer, Dordrecht 3rd edn), pp 363-374.

5. Patronik NA, Ota T, Zenati MA & Riviere CN (2006) Improved traction for a mobile robot traveling on the heart. *Engineering in Medicine and Biology Society, 2006 28th Annual International Conference of the IEEE*: 339-342.

6. Martin RW & Johnson CC (1989) Design characteristics for intravascular ultrasonic catheters. *Int J Cardiac Imag* 4: 201-216.

7. Dhir V, Castle J & Catton I (1977) Role of taylor instability on sublimation of a horizontal slab of dry ice. *J Heat Trans-T ASME* 99: 411-418.

8. Consiglieri L, dos Santos I & Haemmerich D (2003) Theoretical analysis of the heat convection coefficient in large vessels and the significance for thermal ablative therapies. *Phys Med Biol* 48: 4125-4134.

9. Berjano EJ (2006) Theoretical modeling for radiofrequency ablation: State-of-the-art and challenges for the future. *Biomed Eng Online* 5: 24.

SI Figure Legends

Figure S1. (*A*) Layout of an electrode web. (*B*) A magnified view of one pair of electrodes, corresponding to the red dotted box in Fig. S1*A*. (*C*) Cross-sectional diagram of the array. (*D*) Schematic illustration of fabrication and deployment of a cardiac mapping web.

Figure S2. Analytical modelling of serpentine interconnects: (*A*) Geometry of double serpentine interconnects in the *y*-direction. (*B*) Geometry of single serpentine interconnect in the *x*-direction. (*C*) Representative cell of the mapping electrode arrays. (*D*) strain distribution in the polyimide layer of circuits under 10% stretching in both *x*- and *y*-directions. (*E*) Strain distribution in the gold layer of circuits under 10% stretching in both *x*- and *y*- directions. (*F*) Coordinate system for obtaining the displacement of an electrode island (grey) bonded on the surface of the heart (red).

Figure S3. (*A*) Layout of stretchable temperature sensors. (*B*) A magnified view of one pair of electrode design, which corresponds to red dotted box in Fig. S3*A*. (*C*) Cross-sectional diagram of the array.

Figure S4. (*A*) Schematic diagram of leakage current circuitry showing resistor (R_1) in series with R_2, denoting the leakage current escaping and passing through the saline to ground. Leakage current was monitored by measuring voltages across R_1. (*B*) Drawing shows the contact sensor (device under test; DUT) in a bath of saline. Large amounts of leakage current existed in the case where the voltage across R1 approached the input voltage. Leakage currents were controlled with an isolated power supply to prevent leakage currents from entering the body.

Figure S5. (*A*) Axisymmetric heat conduction model for cryoablation. (*B*) Temperature distribution from the modelling (solid lines) agrees well with experimental measurements (square dots).

Figure S6. (*A*) Temperature recorded during RF ablation. The location of the temperature sensor is at position #2. (*B*) The 3D temperature distribution around the RF probe suggests a lesion size of 4.4 mm and depth of 3.7 mm.

Figure S7. (*A*) Layout of a strain gauge web. (*B*) A magnified view the design, corresponding to the red dotted box in Fig. S7*A*. (*C*) Cross-sectional diagram of the array.

Figure S8. (*A*) Change of resistance as a function of uniaxial tensile strain for longitudinal, diagonal and transverse resistors. The gauge factor of the longitudinal resistor is 0.23. *(B)* Response of a longitudinal strain gauge under cyclic uniaxial stretching up to 30%.

Figure S9. (*A*) Schematic drawing of *in vitro* testing with impedance-based contact sensors placed in contact with raw chicken breast meat. (*B*) The results highlight differences detected with contact sensors on wet tissue versus saline.

Figure S10. Material and geometric properties of the contact sensor web device for mounting on a balloon catheter.

Figure S11. (*A*) Circuit diagram of 16-channel contact sensing array. Voltages were measured across the same two terminals where constant current was applied (1-100 kHz). (*B,C*) Photographs of National Instruments data acquisition system with impedance analysis hardware (red circle) and control software running in Labview.

Figure S12. (*A*) Superposition method to obtain the strain in the gauge. (*B*) Interfacial shear stress between the gauge and the substrate for the problem in the bottom frame of Fig. S12*A*. (*C*) Cross-sectional diagram of the gauge (PI in golden and silicon in grey). (*D*) Strain distribution under the Si NM strain gauge for applied strain of 10%.

Figure S13. (*A*) Bending tests of the strain gauges. (*B*) Strain gauge web laminated on raw chicken breast meat under uniaxial tension. (*C*) *In vitro* stretching experiment on chicken. No slippage occurred as the applied strain increased up to ~20%.

Figure S14. End-on view of a device in its deflated state (left) and corresponding schematic cross-sectional illustration (middle). The deformed shape under deflation obtained by both analytical modeling and FEA (right).

Supporting Information Table S1

	Tensile stiffness (N/m)	Theory	FEA
Without silk	x-direction	17.6	16.9
	y-direction	15.0	14.7
With silk	x-direction	7.0E4	7.0E4
	y-direction	7.0E4	6.9E4

Table S1 Comparison between analytical and FEA results for tensile stiffness

Supporting Information Table S2

	Bending stiffness (N-m)	**Theory**	**FEA**
Without silk	x-direction	3.7E-10	3.2E-10
	y-direction	2.8E-10	2.7E-10
With silk	x-direction	4.3E-6	4.7E-6
	y-direction	4.3E-6	4.8E-6

Table S2 Comparison between analytical and FEA results for bending stiffness

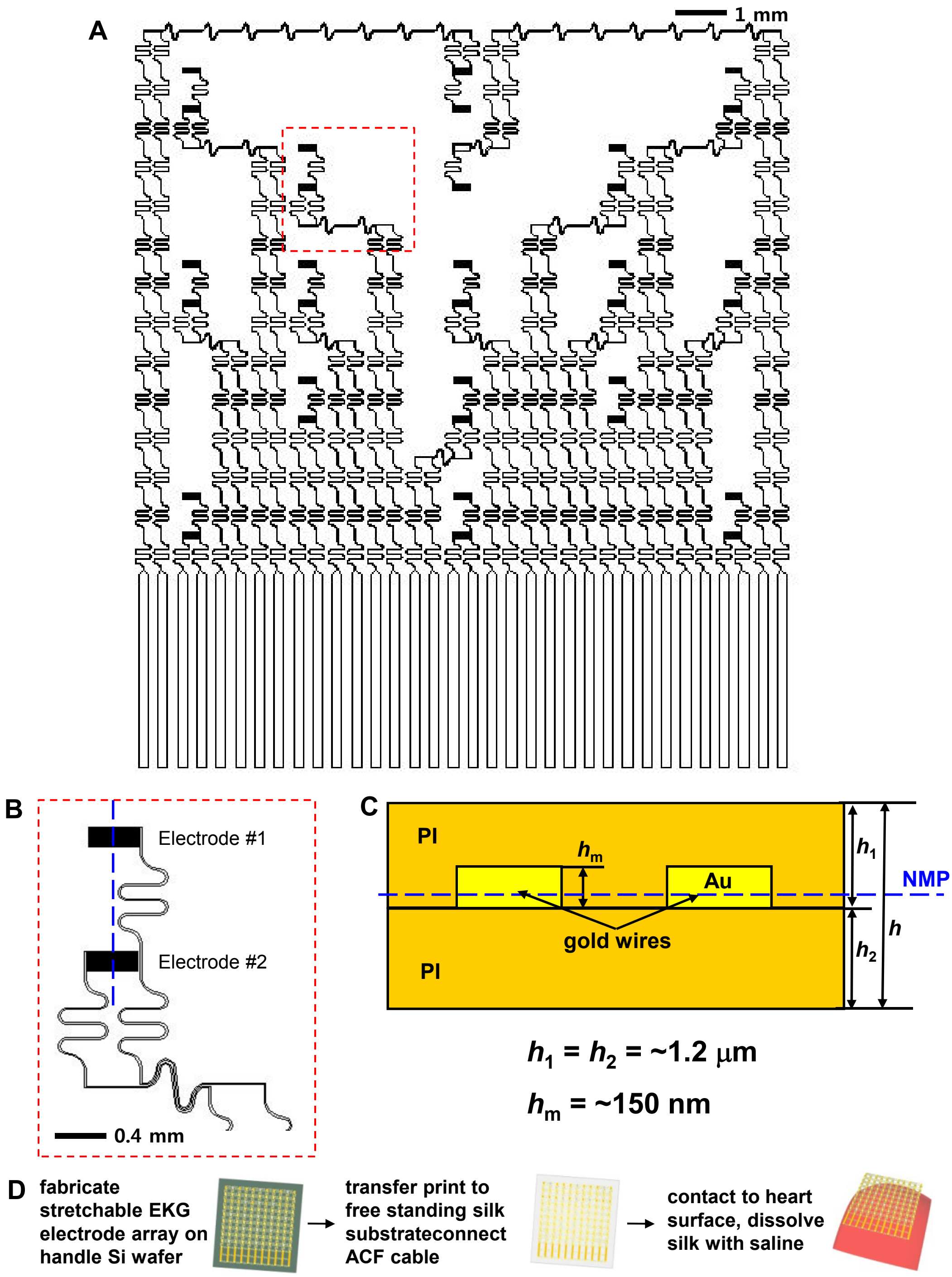
A
1 mm
B
Electrode #1
Electrode #2
0.4 mm
C
PI
h_m
Au
h_1
NMP
h
h_2
gold wires
PI
$h_1 = h_2 = \sim 1.2\ \mu m$
$h_m = \sim 150\ nm$
D
fabricate stretchable EKG electrode array on handle Si wafer
transfer print to free standing silk substrateconnect ACF cable
contact to heart surface, dissolve silk with saline

Figure S1

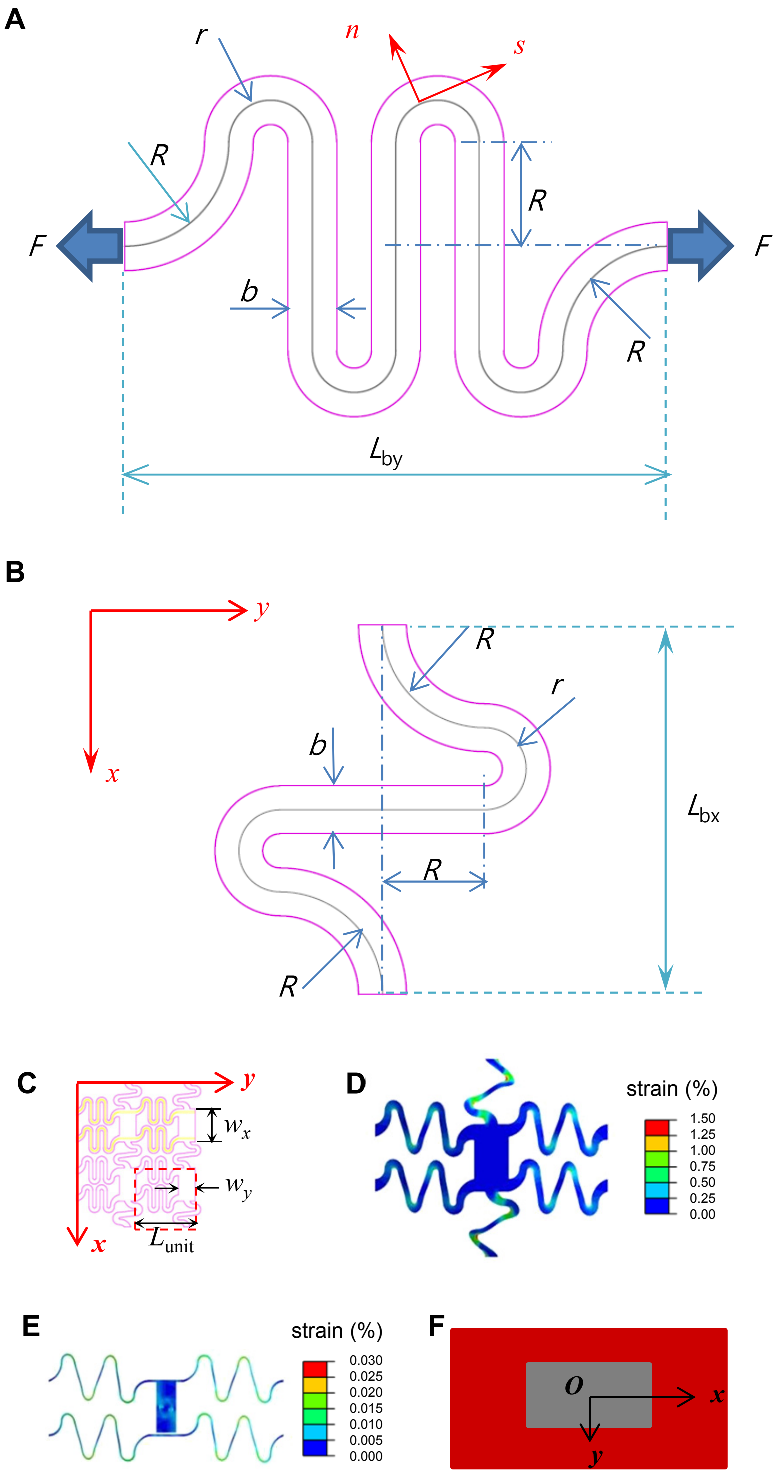
A
r
n
s
R
R
F
F
b
R
L_by
B
y
x
R
r
b
R
L_bx
R
C
y
w_x
w_y
x
L_unit
D
strain (%)
1.50
1.25
1.00
0.75
0.50
0.25
0.00
E
strain (%)
0.030
0.025
0.020
0.015
0.010
0.005
0.000
F
o
x
y

Figure S2

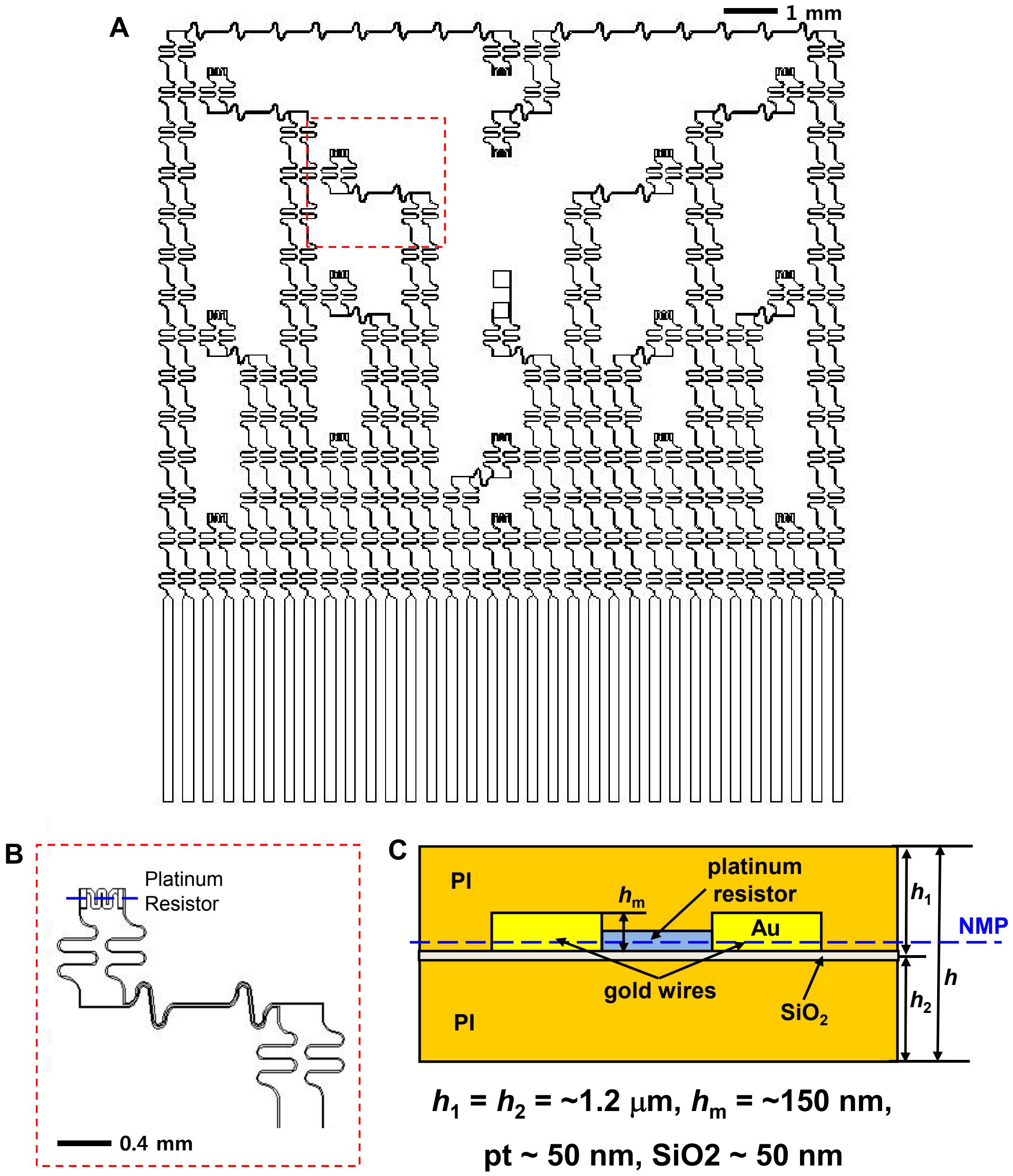

$h_1 = h_2 = \sim 1.2\ \mu m$, $h_m = \sim 150$ nm,

pt ~ 50 nm, SiO2 ~ 50 nm

Figure S3

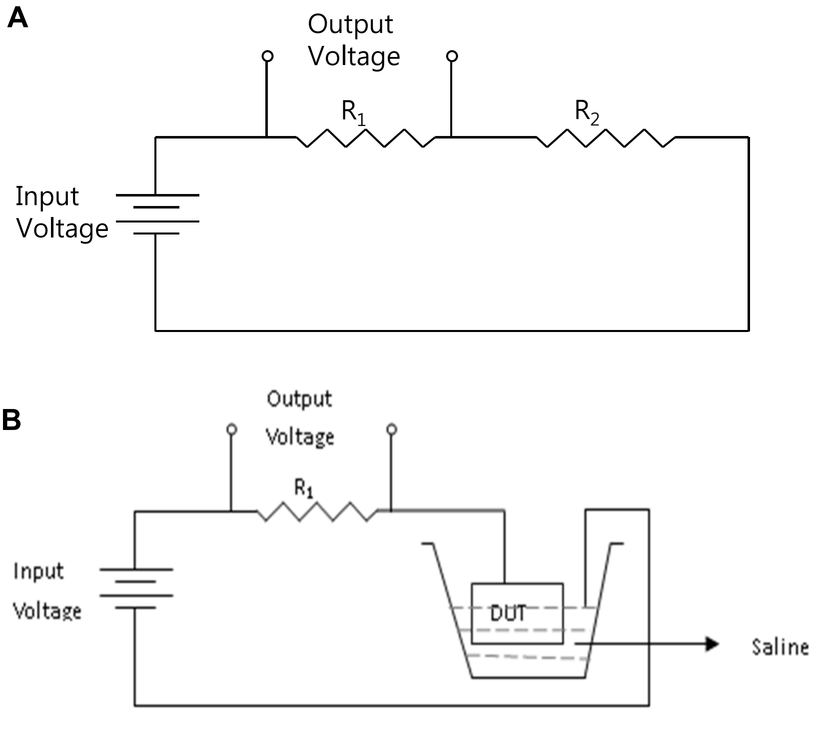
A
Output
Voltage
R1
R2
Input
Voltage
B
Output
Voltage
R1
Input
Voltage
DUT
Saline

Figure S4

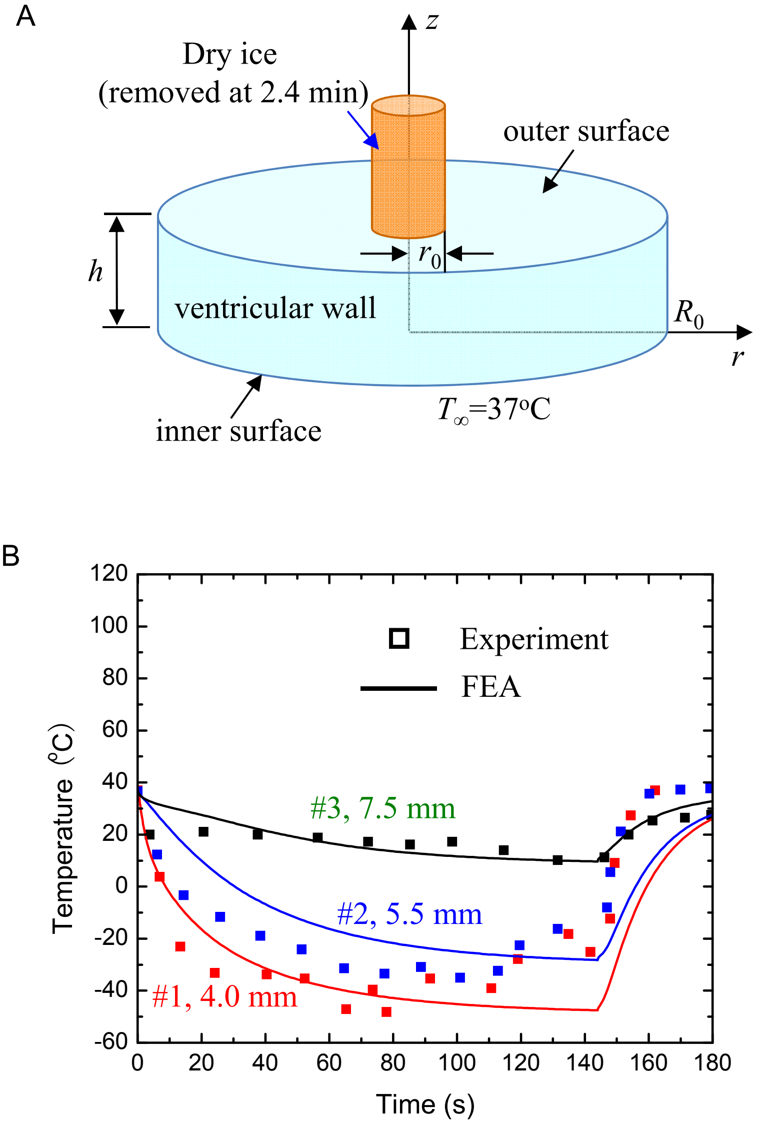
A
z
Dry ice
(removed at 2.4 min)
outer surface
h
r_0
ventricular wall
R_0
r
inner surface
T_∞=37°C
B
Experiment
FEA
#3, 7.5 mm
#2, 5.5 mm
#1, 4.0 mm
Temperature (°C)
Time (s)
120
100
80
60
40
20
0
-20
-40
-60
0
20
40
60
80
100
120
140
160
180

Figure S5

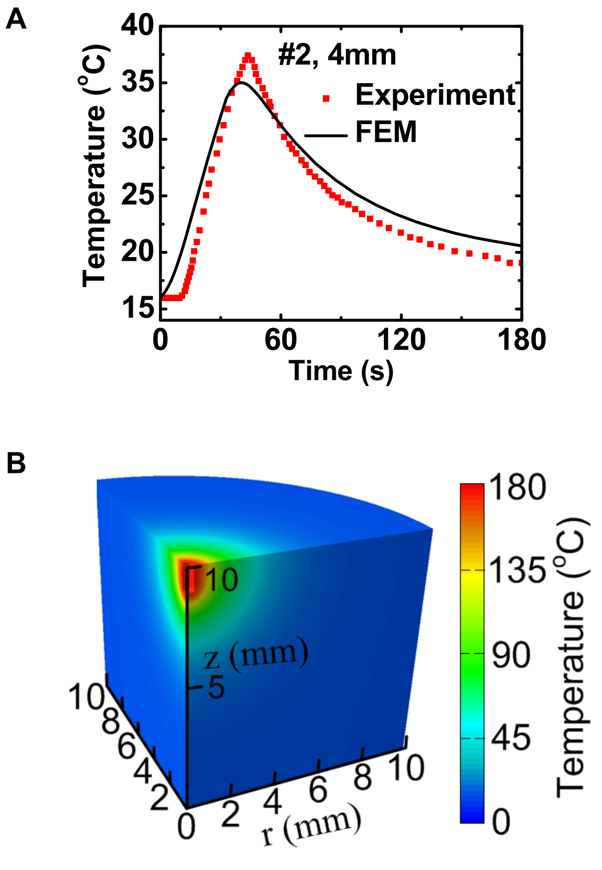A
40
35
30
25
20
15
Temperature (°C)
0
60
120
180
Time (s)
#2, 4mm
Experiment
FEM
B
10
z (mm)
5
10
8
6
4
2
0
2
4
6
8
10
r (mm)
180
135
90
45
0
Temperature (°C)

Figure S6

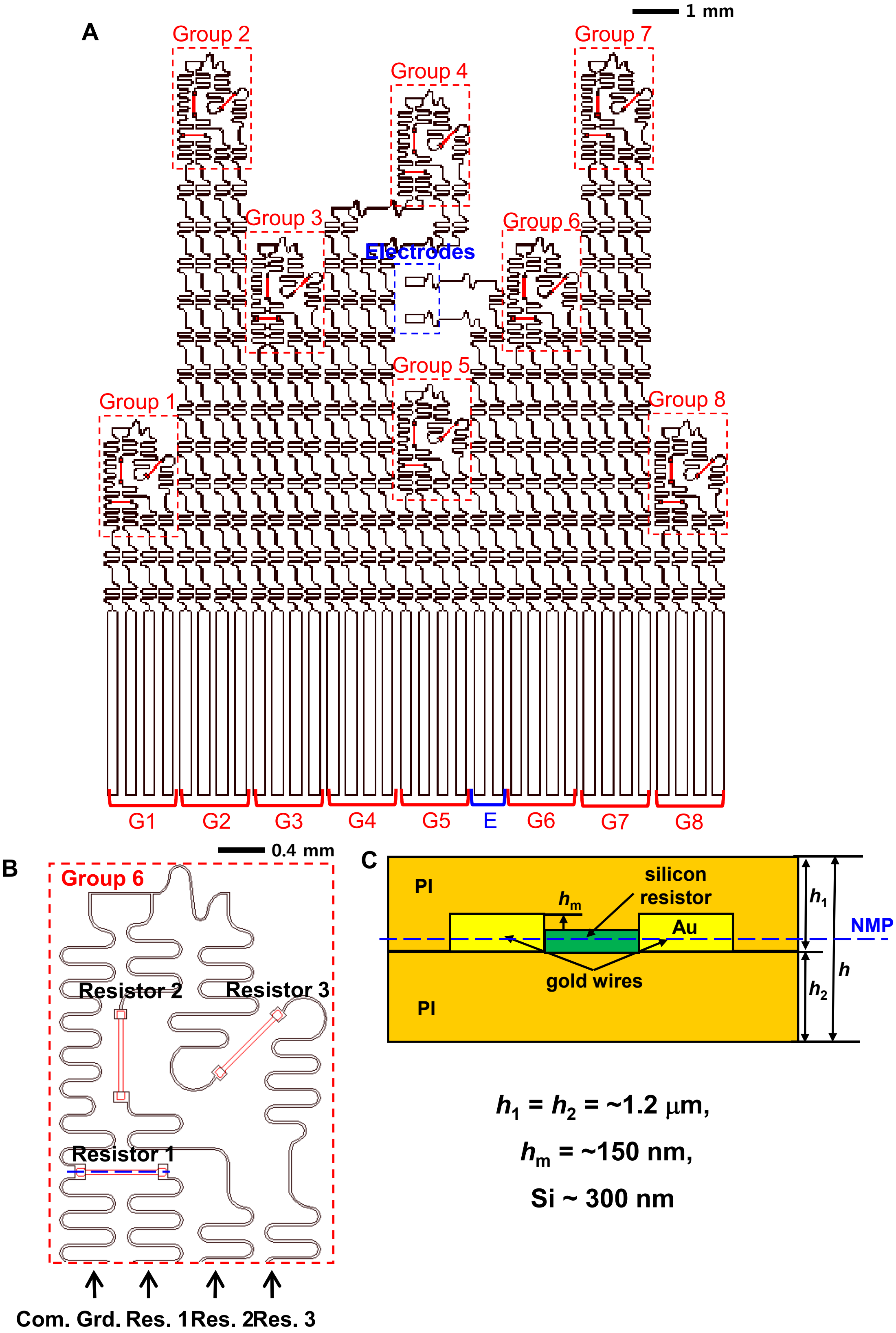

$h_1 = h_2 = \sim 1.2\ \mu m$,

$h_m = \sim 150\ nm$,

Si ~ 300 nm

Figure S7

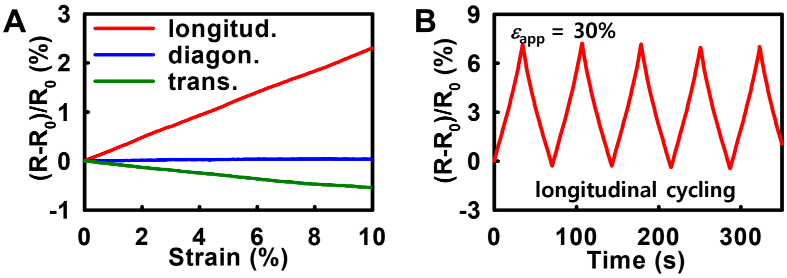
A
3
2
1
0
-1
(R-R0)/R0 (%)
longitud.
diagon.
trans.
0
2
4
6
8
10
Strain (%)
B
9
6
3
0
-3
(R-R0)/R0 (%)
εapp = 30%
longitudinal cycling
0
100
200
300
Time (s)

Figure S8

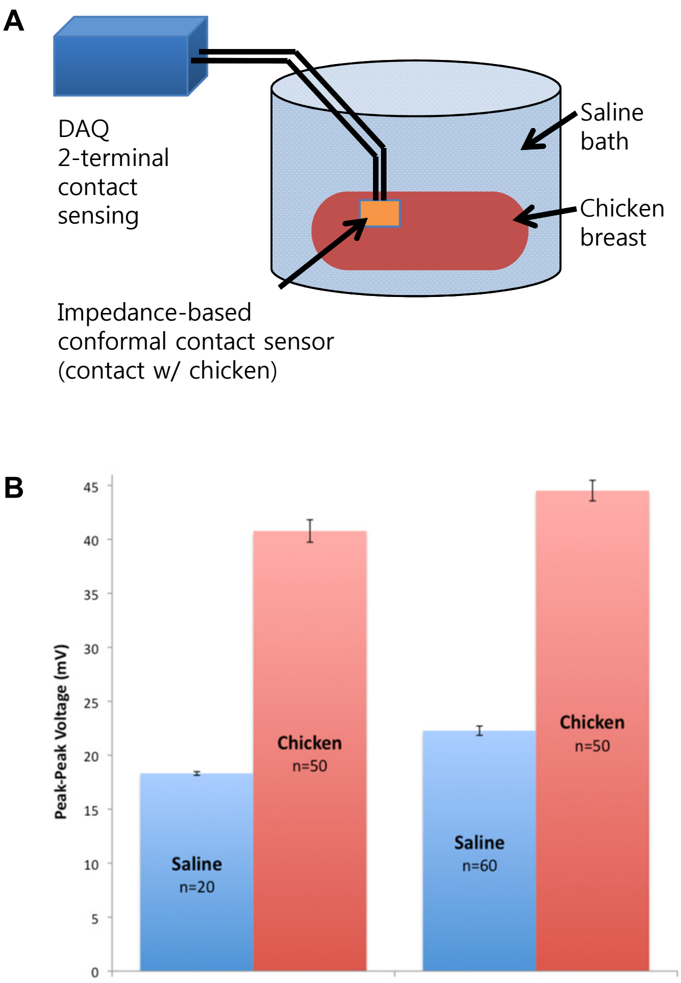
A
DAQ
2-terminal
contact
sensing
Saline
bath
Chicken
breast
Impedance-based
conformal contact sensor
(contact w/ chicken)
B
Peak-Peak Voltage (mV)
45
40
35
30
25
20
15
10
5
0
Saline
n=20
Chicken
n=50
Saline
n=60
Chicken
n=50

Figure S9

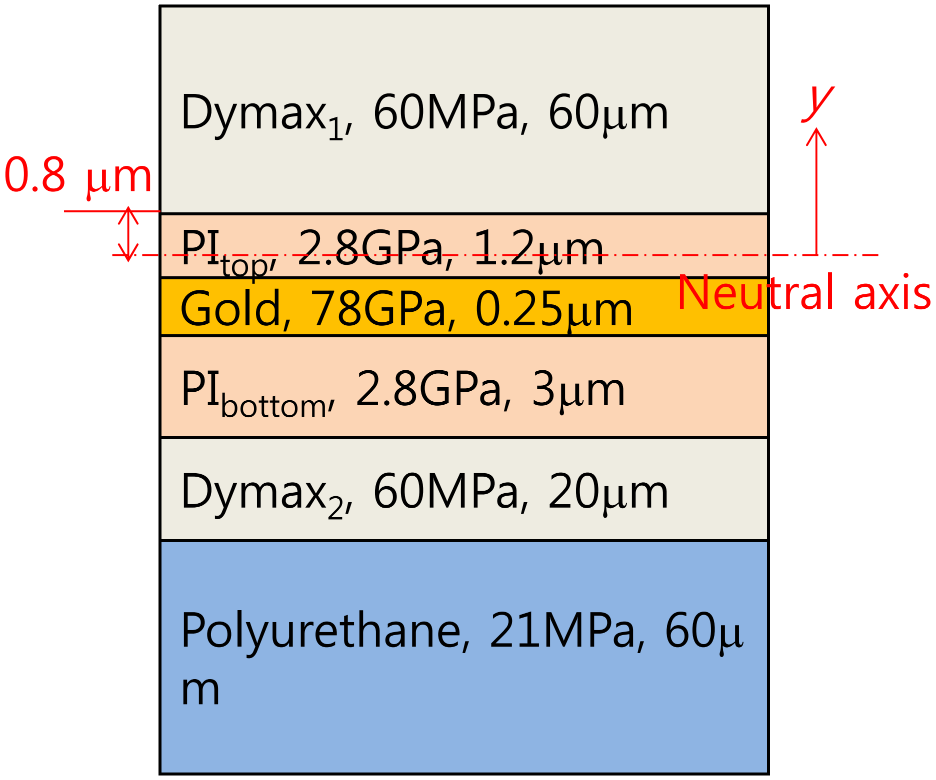
Dymax$_1$, 60MPa, 60μm
y
0.8 μm
PI$_{top}$, 2.8GPa, 1.2μm
Gold, 78GPa, 0.25μm
Neutral axis
PI$_{bottom}$, 2.8GPa, 3μm
Dymax$_2$, 60MPa, 20μm
Polyurethane, 21MPa, 60μm

Figure S10

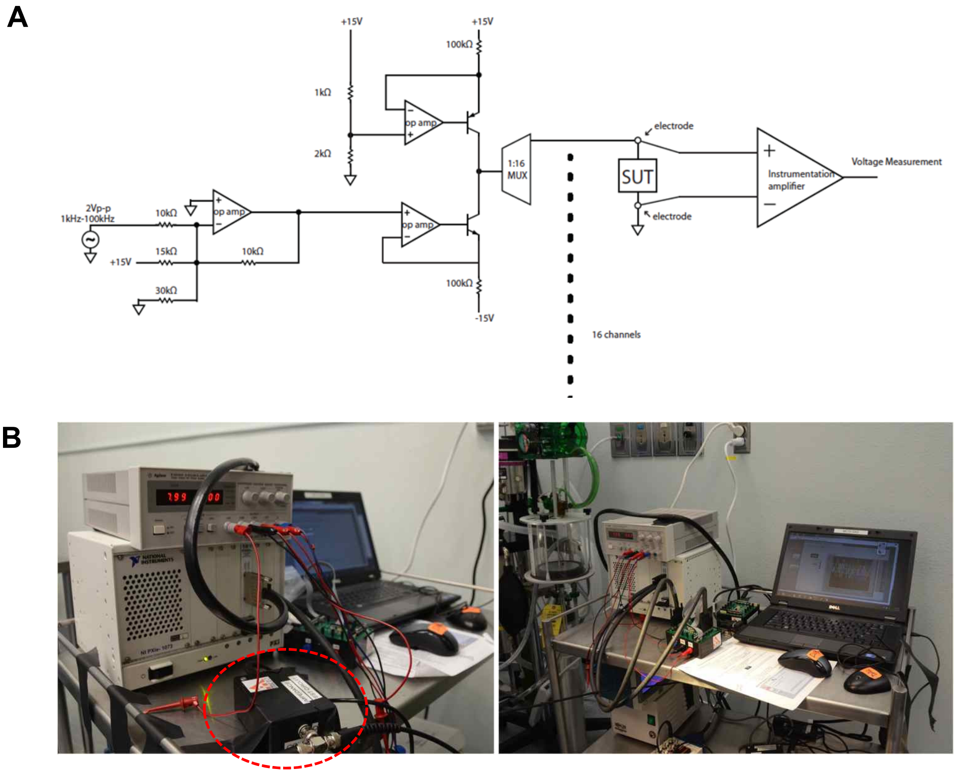

- Custom National Instruments data acquisition system (NI PXI-6289)
- Impedance analysis at 1 kHz, 10 kHz, 100 kHz
- Control software in LABVIEW
- Single-channel analog inputs, 18-bits

Figure S11

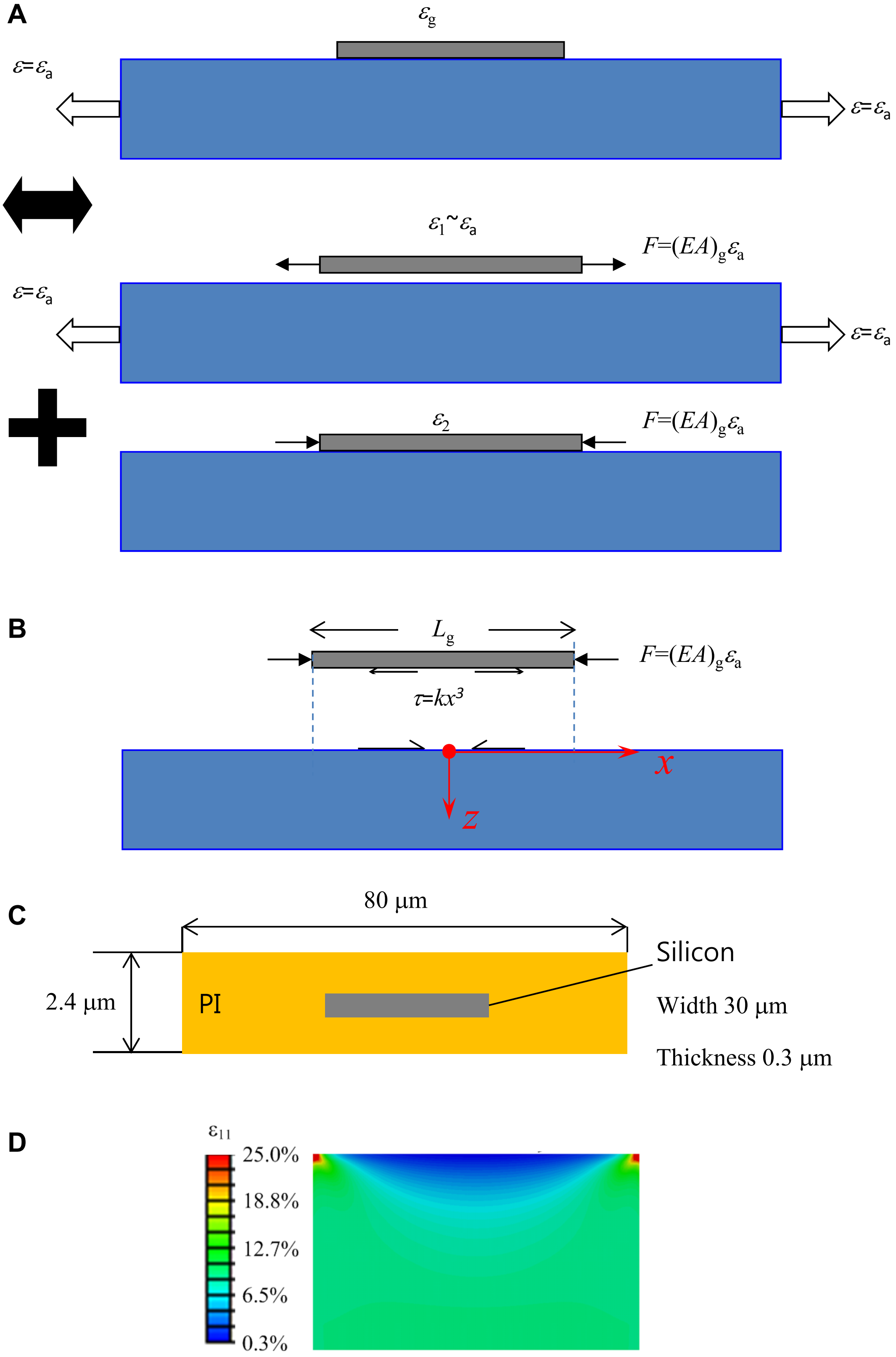
A
ε_g
$\varepsilon=\varepsilon_a$
$\varepsilon=\varepsilon_a$
$\varepsilon_1 \sim \varepsilon_a$
$F=(EA)_g\varepsilon_a$
$\varepsilon=\varepsilon_a$
$\varepsilon=\varepsilon_a$
ε_2
$F=(EA)_g\varepsilon_a$
B
L_g
$F=(EA)_g\varepsilon_a$
$\tau=kx^3$
x
z
C
80 μm
Silicon
2.4 μm
PI
Width 30 μm
Thickness 0.3 μm
D
ε_{11}
25.0%
18.8%
12.7%
6.5%
0.3%

Figure S12

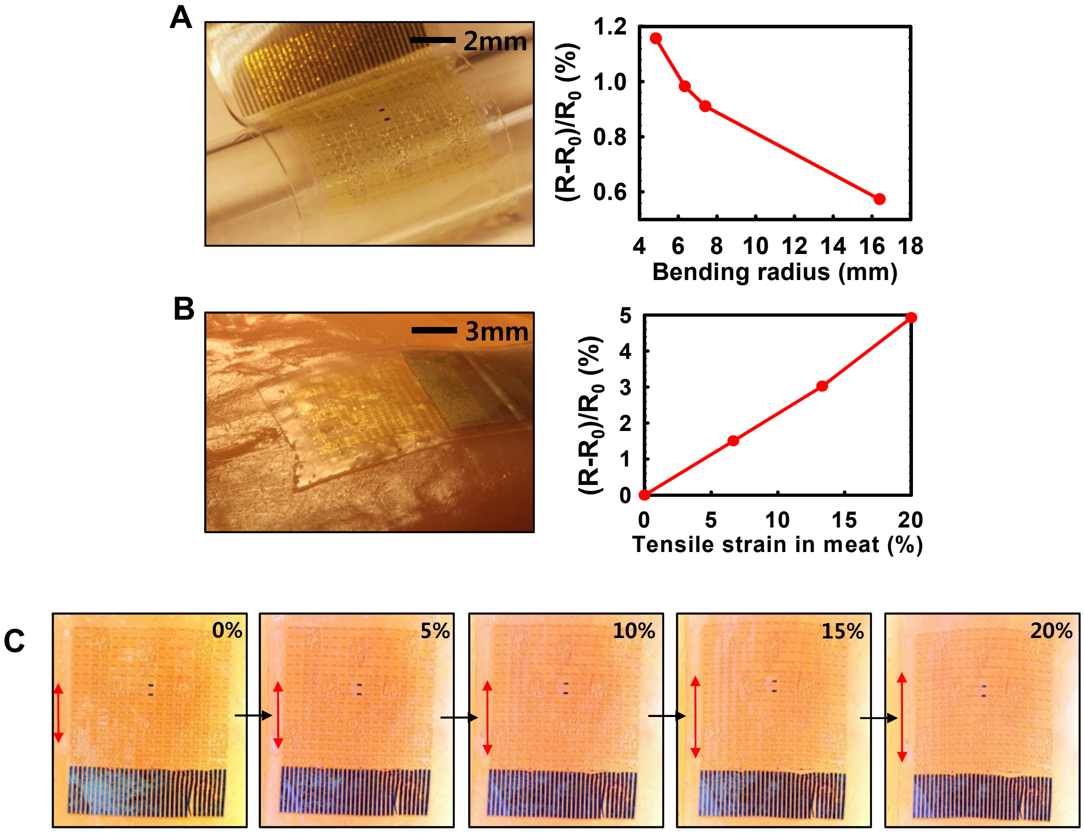
A
2mm
(R-R0)/R0 (%)
1.2
1.0
0.8
0.6
4
6
8
10
12
14
16
18
Bending radius (mm)
B
3mm
(R-R0)/R0 (%)
5
4
3
2
1
0
0
5
10
15
20
Tensile strain in meat (%)
C
0%
5%
10%
15%
20%

Figure S13

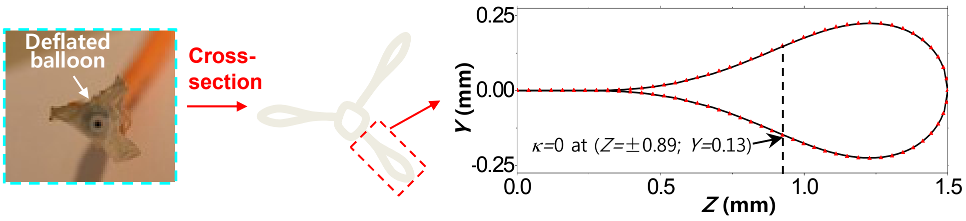
Deflated balloon
Cross-section
0.25
0.00
-0.25
Y (mm)
0.0
0.5
1.0
1.5
Z (mm)
$\kappa=0$ at ($Z=\pm0.89$; $Y=0.13$)

Figure S14